Proc. Lunar Planet. Sci. Conf. 9th (1978), p. 3843–3875.
Printed in the United States of America

Experimental studies of oblique impact*

DONALD E. GAULT**
California Institute of Technology, Pasadena, California 91125

JOHN A. WEDEKIND
NASA, Ames Research Center, Moffett Field, California 94035

"Pelted with star-dust, stoned with meteor-balls-"
R. A. Proctor, 1878

"The number of those falling—having an incidence angle less than any given angle i is equal to $\sin^2 i$."
G. K. Gilbert, 1893

Abstract—Meteoritic materials most probably impact planetary bodies along oblique trajectories inclined less than 45° above their surfaces. Laboratory studies of hypervelocity impacts against rock and particulate media are presented that indicate important effects of obliquity on crater size, shape, and ejecta distribution. The effects are particularly important to crater size-frequency analyses and geologic interpretations of crater formations. Impacts at shallow incidence, which are not uncommon, lead to ricochet of the impacting object accompanied with some entrained excavated materials at velocities only slightly reduced from the pre-impact value.

INTRODUCTION

In his classic paper Gilbert (1893) has shown for a non-gravitating body (i.e., zero mass), and subsequently extended by Shoemaker (1962) to gravitating bodies, that the most probable angle of impact is 45° (no atmospheric deceleration). One of every two events occurs at an angle less than 45° (90° = vertical incidence), one of every four events occurs at less than 30°, and three of every 100 events occurs at angles less than 10°. These probabilities are based on an assumption of an isotropic source of impacting objects—a condition which is not realized at the present time nor, probably, in the past for planetary environments—and the predictions are a conservative lower limit approximation for the actual probabilities, especially for the large meteoritic masses for which topographic shielding is not significant. The concentration of meteoritic bodies near the ecliptic plane in orbits with low inclinations causes the actual probabilities to skew to smaller angles of incidence with the end result of increasing the frequency of shallow angle trajectories with respect to an isotropic flux model. No quantitative assessment of the enhanced probability for smaller trajectory angles is readily possible because results depend critically on

*Contribution No. 3060, Division of Geological and Planetary Science, California Institute of Technology, Pasadena, California 91125.

**Permanent address: Murphys Center of Planetology, 350 Main Street, P.O. Box 833, Murphys, California 95247

the orbital parameters of the impacting flux, but it is to be noted that the "top" or polar regions of the planetary bodies should have experienced fewer steep or near vertical trajectory impacts in comparison to equatorial regions.

Except for obvious elongate craters and asymmetrical ray systems and distributions of inferred melt and ejecta deposits (e.g., Moore, 1968, 1976; Howard and Wilshire, 1975; Hawke and Head, 1977), many effects and results of oblique impact trajectories remain unrecognized or poorly defined and understood. It is commonly assumed either tacitly or for reasons of simplicity, convenience, and/or lack of information that impact craters have been formed under conditions corresponding to vertical incidence. Probably the major contributing factor in this neglect of obliquity effects (other than a paucity of experimental impact data) has been the general acceptance of explosive cratering and its associated large data base as being analogous and applicable to impact events (e.g., Shoemaker, 1962; Baldwin, 1963; Roddy, 1977). Although there is a firm basis for the analogy in many respects, the comparison neglects an important difference between explosions and impact events; i.e., explosions represent an energy release from a point source whereas impacts effectively release energy along a line source of the path of projectile penetration. For near vertical incidence the difference between point and line sources is minimal as clearly evidenced by the experimental results reported by Oberbeck (1971). However, as trajectory angle is reduced, differences between point and line sources become extreme and lead to significant changes in the cratering processes, differences which probably can be examined only experimentally at the present time and then only at small laboratory scale.

It is interesting that laboratory studies of oblique impacts for lunar (and planetary) application date back to at least Gilbert (1893) who mentions, but gives no data, performing impact experiments to determine effects of obliquity on crater circularity by "dropping" or "throwing" projectiles of "mud" or "plastic clay" into targets of similar materials. Undoubtedly many other similar low velocity experiments have been performed in the interim employing a variety of media (e.g., Sabaneyev, 1953), but among the first "high" velocity experiments may be those carried out by Barringer in connection with his investigation of the Arizona Meteor Crater (Barringer, 1927). Again, the objectives were the effects of obliquity on crater circularity, but in this case a rifle was fired into mud. Probably the first true hypervelocity oblique impacts were conducted by Rinehart and White (1951) using iron and aluminum projectiles with velocities up to 4.7 km/sec to study crater shape in plaster-of-paris targets. There has since followed many systematic investigations of oblique impact into metals (e.g., Partridge and Van Fleet, 1958; Summers, 1959; Bryan and Pugh, 1962), but comparable studies for geologic applications are believed limited to those performed in recent years on the Vertical Gun Ballistic Range (VGBR) at the NASA's Ames Research Center. It is the purpose here to summarize the VGBR results for a better understanding and appreciation of obliquity effects. Some of these results are previously unreported but many have been presented in earlier publications (Gault *et al.*, 1965, 1972, 1974; Gault, 1973, 1974; Fechtig *et al.*, 1972; Fudali and Chapman, 1975).

Experimental Procedures

The VGBR facility consists of a 2.5 m diameter by a 3 m high impact chamber that is straddled by a large A-frame on which light-gas guns (Charters and Curtis, 1962; Curtis, 1964) and conventional powder guns can be mounted. Rotation of the A-frame up over the impact chamber permits launching projectiles against horizontally positioned targets through ports into the chamber at angles from the horizontal ($\theta = 0°$) to vertical incidence ($\theta = 90°$) in increments of 15°. Impact angles between 0° and 15° for particulate targets were obtained by tilting the targets, but in no case exceeding a tilt angle of 7.5°.

With few exceptions all data were obtained with an ambient pressure in the chamber between 0.1 and 1.0 Torr air; in no case did the pressure exceed 5 Torr, except one series of impacts into granites for which $\theta = 90°$. Projectile velocities varied from 0.05 to 7.2 km/sec.

Most of the presented results were obtained using spherical projectiles of aluminum or pyrex or right-circular cylindrical projectiles (2/3 caliber long) of lexan, but included are some observational results based on polyethylene, lead, iron, and tungsten spheres. Sphere diameters ranged from 1.6 to 12.5 mm; cylindrical diameters were .30 caliber (7.6 mm) and 20 mm. All spherical projectiles were launched encased in cylindrical lexan 'sabots' to prevent mutual abrasion of the launch barrels and projectiles. The sabots were cut into two halves along their axis of symmetry. Centrifugal forces induced by rifling in the barrels acted to deflect the halves away from the projectile trajectory into a "catcher" and prevent their entry into the impact chamber. Subsequently, sub-microsecond spark shadowgraphs of the projectile, synchronized with 10-MHz time-interval meters, were obtained to provide a time-distance record for velocity determinations and, also, to provide a check on the physical integrity of the projectiles. Precision of the velocity determinations was ± 0.01 km/sec. In those experiments specifically concerned with the behavior of the ejecta plume and its final disposition on the reference surface around the crater, an explosively driven shutter (closure time approximately 100 μsec) was employed to trap propellant gases uprange of the impact chamber and prevent any aerodynamic disturbances of the ejecta.

Results are presented for three different target materials. For a dense crystalline rock, a Sierra Nevada granite, Raymond, California, was employed. Bulk density of this granite is 2.56 ± 0.05 g/cm^3 and the unconfined, uni-axial compressive strength varied from 1.7 to 2.5 kbars. However, two particulate media, quartz sand and pumice powder, provide the basis for most of the results herein. Median grain size for the quartz was approximately 0.5 mm with more than 90% between 0.2 and 0.7 mm. The pumice target material was obtained from Mono Craters, California, using all pumice passing through a U.S. No. 140 mesh screen (<105 μm). Bulk densities of these two particulates averaged 1.7 and 1.05 g/cm^3, respectively.

In contrast to the virtually cohesionless properties of the quartz, the pumice material in the low pressure environment of the impact chamber exhibited some cohesion, which served to form small clots of pumice within the main sheet of ejecta plumes. This cohesive tendency of the pumice proved to be an advantage for preserving and documenting the shapes and areal densities of the main ejecta deposits around their craters. The pumice "stuck" in place whereas the quartz sand bounced and rolled across the reference surface smearing out and obliterating the main ejecta patterns, a behavior that dictated the use of the cellular reference surface in the experiments reported by Stöffler *et al.* (1975).

Photographic records of crater formation were taken of some impacts using Nova high-speed cameras framing at rates of 7000 to 10,000 frames/sec. Most records were obtained viewing the event only from the side along the reference surface, but some records were obtained with simultaneous orthogonal views from the side and from the top of the impact chamber looking down into the crater.

It should be noted that with consideration of the decrease in the effective strength of rock at scales greater than the laboratory experiments (Gault, 1973), the results for particulate targets are probably the most representative for modeling large planetary cratering events as well as being directly applicable to the smaller scale regolith cratering.

Crater Shape

Changes in the circularity of the craters with oblique incidence, a subject of prime concern to the early investigators, are presented in Figs. 1 and 2. The

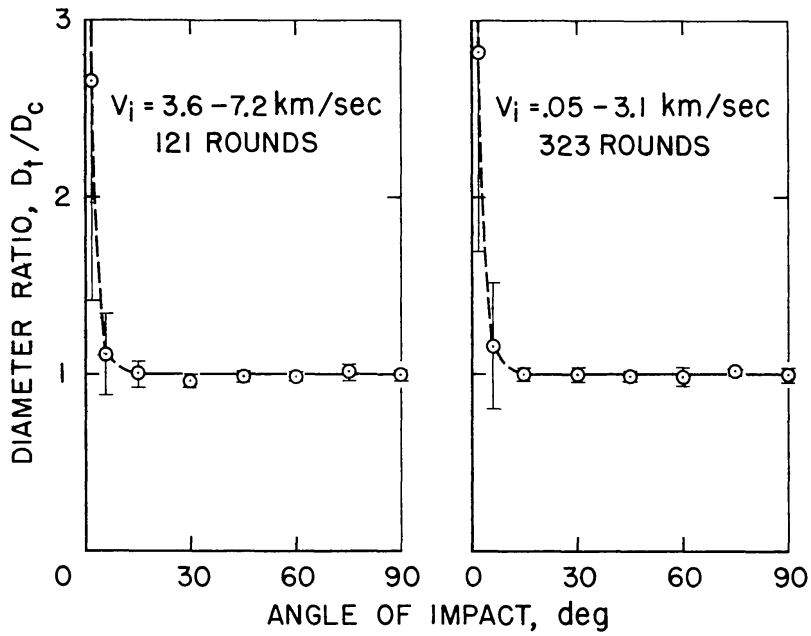

Fig. 1. Effect of oblique impact on circularity of craters formed in non-cohesive quartz sand by aluminum and pyrex spheres and 2/3-caliber, right circular cylinders of lexan. Error bars are standard deviations.

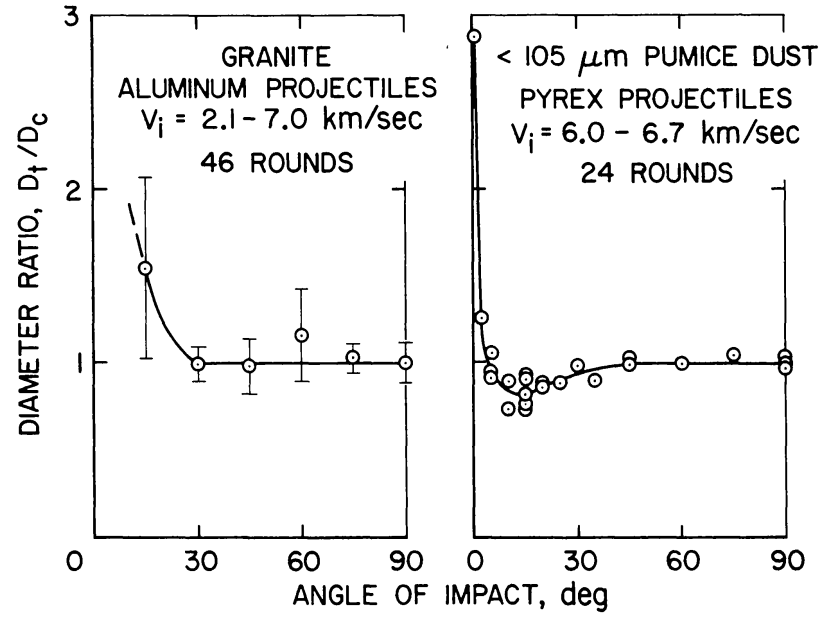

Fig. 2. Effect of oblique impact on circularity of craters formed in granite and pumice dust (<105 μm) by, respectively, aluminum and pyrex spheres. Error bars are standard deviations.

measure of circularity is defined here, for simplicity, to be the ratio D_t/D_c, where D_t is the maximum dimension of the basic crater measured along the path of the projectile trajectory (but excluding the extensive downrange gouges formed at grazing incidences), and D_c is the maximum dimension of the crater taken at right angles to the trajectory path, both quantities with respect to the pre-impact surface.

Craters in all target media remain circular within a few percent for trajectory angles from the vertical to at least $\theta = 30°$. For angles less than about 30° incipient conditions for ricochet are approached and crater geometry then becomes a function of impact velocity and the physical properties of the target/projectile combination. (The subject of ricochet and accompanying phenomena will be discussed in a subsequent section). Craters formed in granite at 15° with aluminum projectiles, which ricochet, are significantly elongate along the trajectory path. For quartz sand targets, marked departure from circular planform occurs only for angles less than about 10°, irrespective of the type of projectile, impact velocity, or occurrence of ricochet. For angles less than 10°, however, the craters in quartz sand become elongated along the path of the projectile with the degree of elongation depending on projectile materials and impact velocity, as illustrated in Figs. 3 and 4. Craters formed in the pumice powder with pyrex projectiles display similar elongation at small angles and, additionally, exhibit an unusual trend between $\theta = 30°$ and 10° when craters become elongated at right angles to the trajectory path; an average of about 15-percent for five craters formed at $\theta = 15°$. The cause for this trend in unknown.

Representative profiles of craters along and across trajectory are shown in Fig. 5 for impacts into the pumice. An interesting characteristic of the profiles, reported previously for craters formed in quartz sand (Gaults *et al.*, 1965) is the development of steeper interior slopes on the uprange wall of the cavities for shallow trajectories ($\theta < 30°$). This obliquity effect is more pronounced with pumice due to its cohesive properties which permit steeper angles of repose. Profiles for craters formed in quartz sand ($\theta = 90°$, 45°, and 15°) are presented in Gault *et al.* (1974).

Figure 6 presents measurements of the depth/diameter ratio for craters in the rock and particulates. Depth d and "apparent" diameter D_a are taken with respect to the undisturbed surface and where $D_a = \frac{1}{2}(D_t + D_c)$ in those cases where the craters depart from circular planform.

Although there is considerable scatter in the data for granite and pumice, the ratio for craters in these materials appears to remain effectively constant even after ricochet and significant crater-planform elongation occurs. In contrast, craters in quartz sand display a small decrease in d/D_a from $\theta = 90°$ to 30° and then a sudden (discontinuous?) decrease occurs after ricochet and elongation takes place. Although the differences are within one sigma limits of the data, the larger decrease for pyrex projectiles relative to aluminum is consistent with their lower density (2.2 vs. 2.7 g/cm^3) and differences in physical properties (lower strength and brittle vs. ductile). Both properties serve to decrease penetration of the projectile into the target which, in turn, is critical for transfering its kinetic energy to the target medium and precluding conditions for ricochet. Results for the

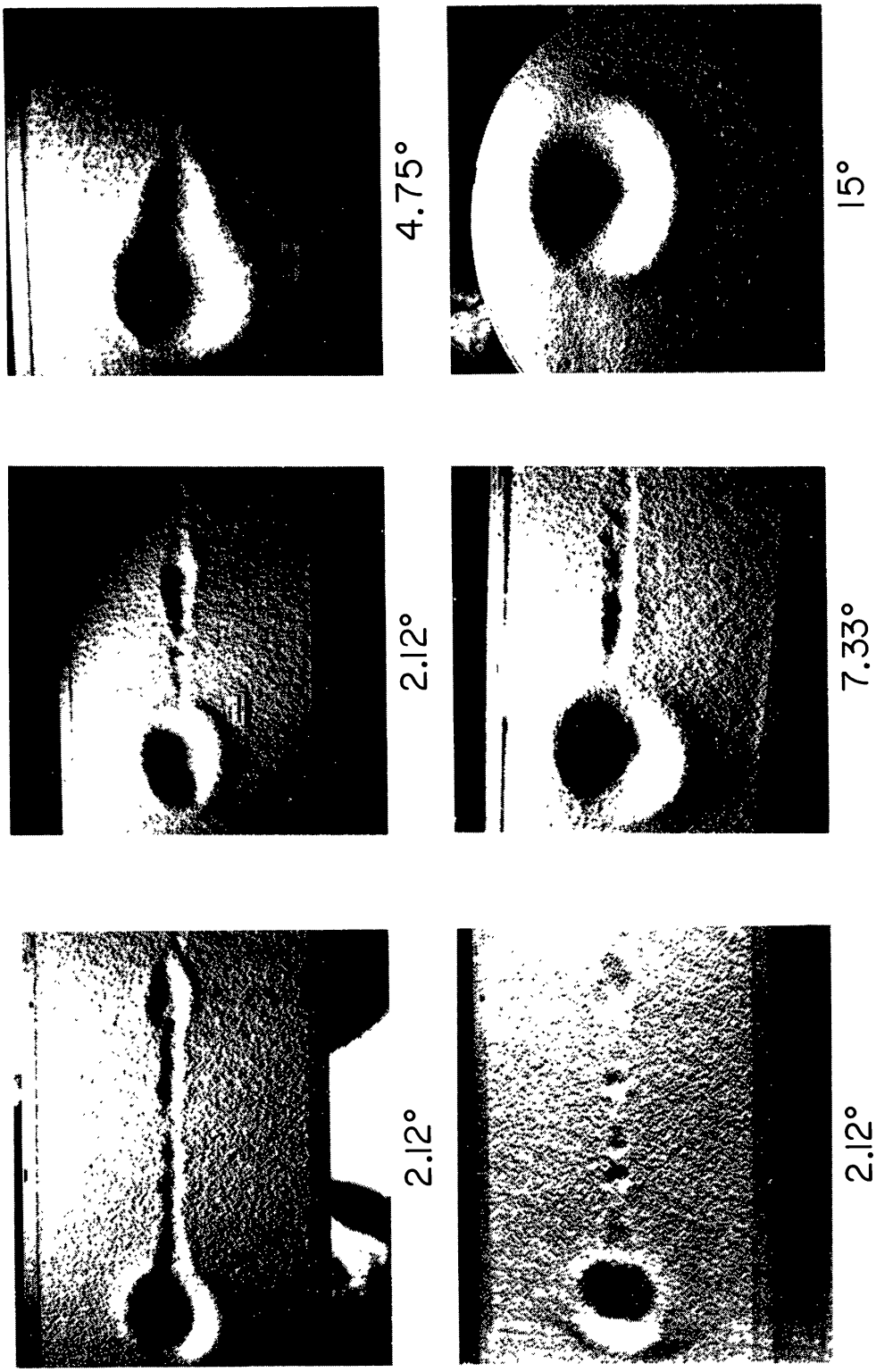

Fig. 3. Craters formed by oblique impacts of pyrex spheres at velocity of approximately 6.4 km/sec into non-cohesive quartz sand. Trajectory from left to right and angles indicated in degrees. Target container is 30 cm wide. Two views on left (θ = 2.12°) are same crater, but with illumination across (top) and along (bottom) path of trajectory to emphasize subtle morphologic characteristics of downrange "cratering".

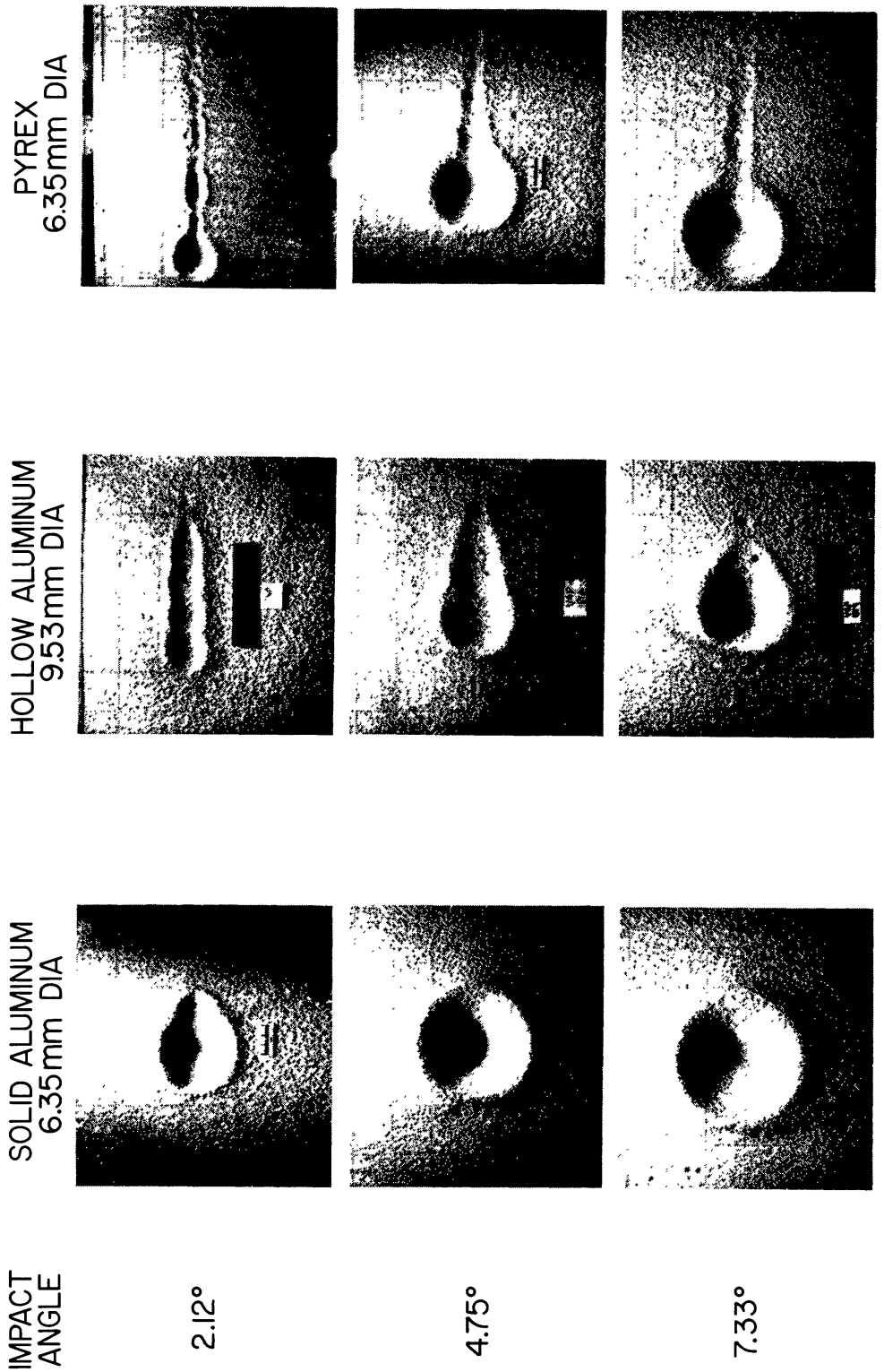

Fig. 4. Effects of physical properties of projectile on craters formed by oblique impacts into non-cohesive quartz sand at velocity approximately 1.7 km/sec. Decreases in strength increase downrange cratering; weaker projectiles produce downrange disturbances at larger values of θ.

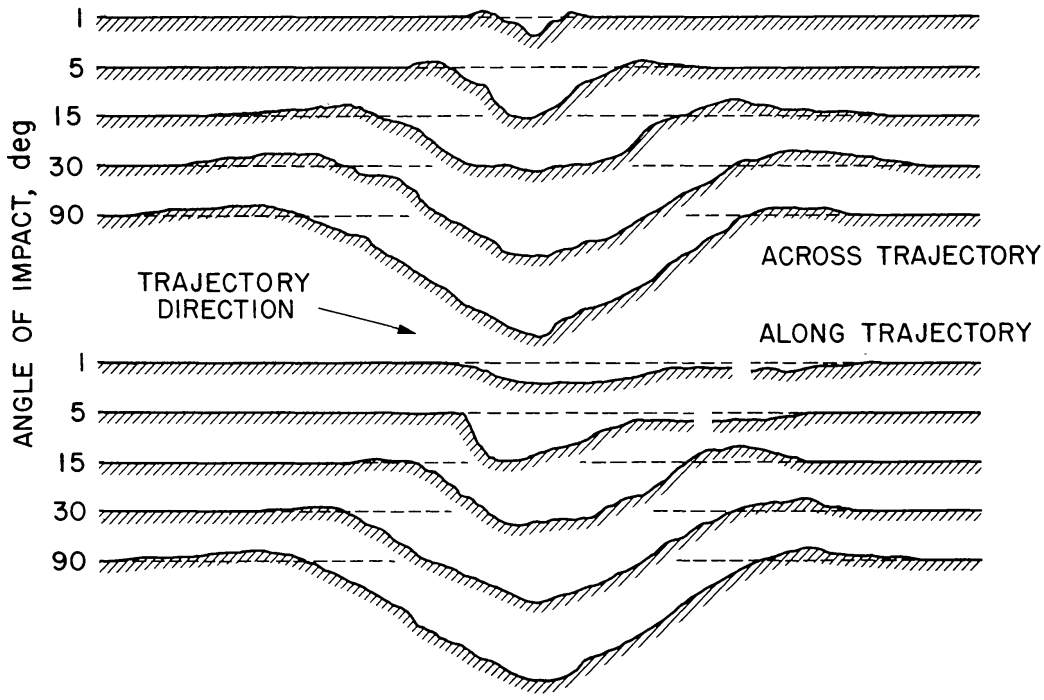

Fig. 5. Geometry of craters formed in pumice dust (<105 μm) by oblique impacts of pyrex spheres at velocity approximately 6.4 km/sec.

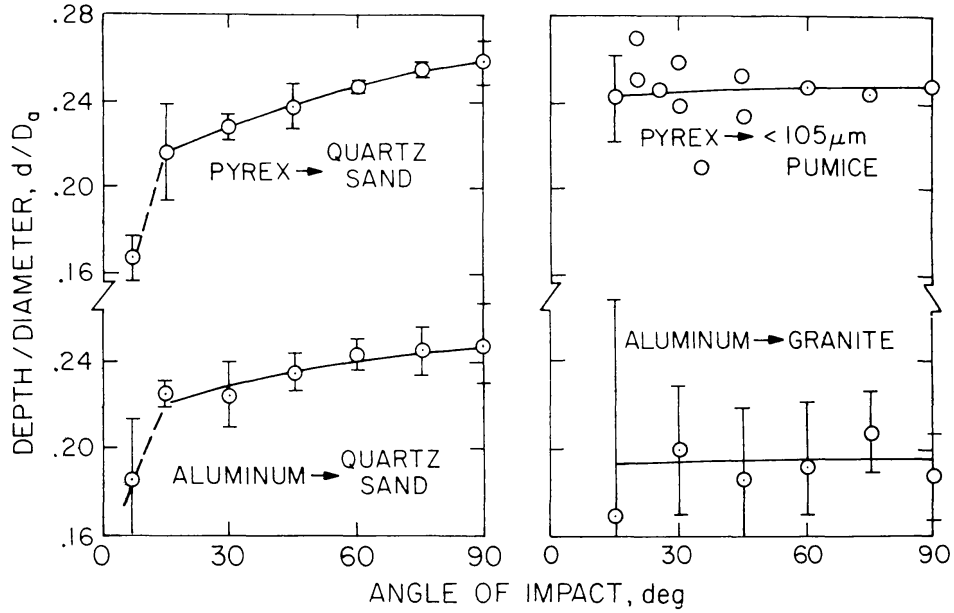

Fig. 6. Variation of crater depth/diameter ratio with trajectory angle for conditions shown in Figs. 1 and 2. Error bars are standard deviations.

pumice craters, for which there is a large density difference between target and projectile, and incomplete data for iron and plastic (lexan and polyethylene) projectiles, support this interpretation.

Crater Size

The diameter of craters decreases with increasing obliquity, all other variables being held constant. But in order to avoid the complications arising from non-circular craters at shallow trajectory angles, the change in crater dimensions with obliquity is more conveniently expressed for subsequent analyses in terms of the mass of target material M_e that is displaced by the impact event ($M_e = \rho_t W$, where ρ_t is the target density and W is the crater volume with respect to the undisturbed surface). Figures 7, 8, and 9 present the displaced masses normalized with the masses displaced at vertical incidence for impact into granite, quartz sand, and pumice powder, respectively. These results indicate a significant difference between the rock and particulate targets. As noted previously (Gault *et al.* 1972; Gault, 1973, 1974), the displaced mass in granite varies as $\sin^2\theta$ whereas the variation for the particulates is proportional to $\sin\theta$. These effects of oblique impact have been generally neglected or overlooked by workers in the past, but they have important ramifications in converting mass-number distributions of impacting objects to crater size-frequency distributions, or vise versa, erosion rates, mass transport, etc.

As shown by Gilbert (1893) and Shoemaker (1962) for an isotropic flux of impacting objects, the differential probability dP for an impact on an angle θ is

$$dP = 2 \sin\theta \cos\theta \, d\theta \tag{1}$$

Accepting this as a reasonable (conservative) approximation for describing the trajectory angle distributions, and introducing the usual formulation for mass-number distribution of the impacting objects

$$N \propto m^{\alpha} \tag{2}$$

(1) and (2) may be combined to give

$$dN \propto m^{\alpha} \sin\theta \cos\theta \, d\theta \tag{3}$$

where dN is the differential number of objects with masses equal to or greater than m which will impact with a trajectory angle θ. Now, if geometric similarity is assumed for the craters for all values of θ, an "average" diameter $D(\theta)$ can be expressed in terms of the displaced mass

$$D^3(\theta) \propto m_e$$

and based on the experimental evidence (Figs. 7, 8, and 9) one may write

$$D^3(\theta) = D^3_{90^\circ} \sin^{\delta}\theta \tag{4}$$

with $\delta = 1$ or 2 depending on the target material. Taking a scaling relationship for the diameter D_{90° at vertical incidence in terms of the impact kinetic energy E in the form

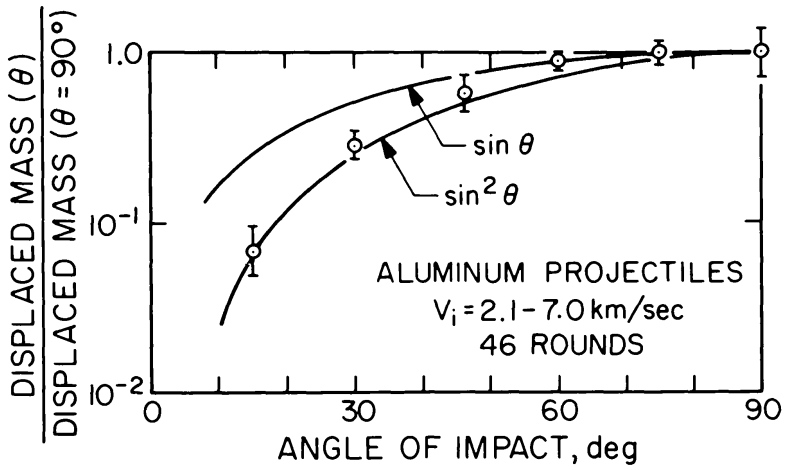

Fig. 7. Effects of oblique trajectory on displaced mass from craters formed in granite by impacts of aluminum spheres. Error bars are standard deviations.

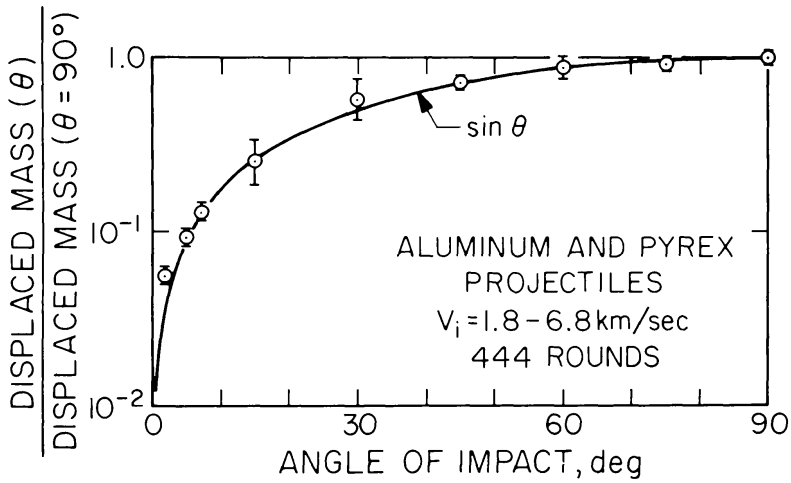

Fig. 8. Effects of oblique trajectory on displaced mass from craters formed in non-cohesive quartz sand by impacts of aluminum and pyrex spheres. Error bars are standard deviations.

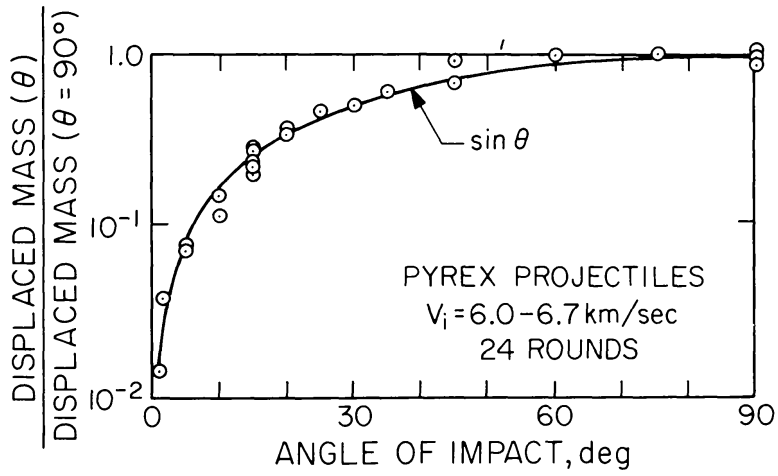

Fig. 9. Effects of oblique trajectory on displaced mass from craters formed in pumice dust (<105 μm) by impacts of pyrex spheres.

$$D_{90°} \propto E^{\beta} \propto (mV^2)^{\beta} \tag{5}$$

and assuming the velocity is constant, elimination of the mass m between (3) and (5) using (4) yields the differential number of craters with diameter D and larger that are produced with impacts having trajectory angles of θ

$$dN \propto D^{\alpha/\beta} \cos\theta \, (\sin\theta)^{1-\frac{\alpha\delta}{3\beta}} \, d\theta \tag{6}$$

Integration over the limits θ = 90° to 0° gives the total number of craters N(θ) of diameter D and larger formed by all trajectories

$$N(\theta) \propto \frac{3\beta}{6\beta - \alpha\delta} D^{\alpha/\beta} \tag{7}$$

Normalizing (7) with the number produced when obliquity effects are neglected (i.e., δ = 0) and it is assumed that all impacts occur from vertical trajectories one obtains

$$N(\theta) = \frac{6\beta}{6\beta - \alpha\delta} N_{90°} \tag{8}$$

Because α is negative, Eq. (8) expresses a reduction in the crater population when the effects of oblique trajectories are taken into consideration relative to the usual assumption that events occur only at θ = 90°. Detailed evaluation and discussion of this result is beyond the scope here, but we note that for small scale impacts into rock Eq. (8) indicates that obliquity conservatively reduces the apparent crater population by a factor of 2.1; in regolith-type materials the factor is in the range of 1.5–1.7, and for major events is greater than 1.7 and may approach 2.0. Conversely, given a crater size-frequency distribution the number of objects of mass m or greater required to form the distribution would be under estimated by these same factors. It is emphasized that these estimates are based on an assumed isotropic source of impacting objects; preliminary considerations suggest that a concentration of low inclination orbits near the ecliptic plane could increase these estimates by at least 50-percent.

Ejecta Distribution

The ejection of target material from craters in rock or particulates departs very little from the axial symmetric conditions of vertical impacts (and explosions) until θ is less than 45°. The principal changes caused by increasing obliquity are a gradual enhancement of the highest-velocity components of ejecta into downrange azimuths (ray elements?) and a slowly increasing downrange tilt in the axis of symmetry of the conical-shaped plume of the lower-velocity components of ejecta which comprise the main mass displaced by the impact. The tilt in axis of symmetry is caused by steeper angles of ejection along the uprange wall of the enlarging cavity and apparently, as discussed previously, results in steeper interior slopes of the uprange wall of the final crater.

Because the major fraction of ejecta mass from the laboratory craters in rock consists of large, irregular shaped spall plates (Gault *et al.*, 1963; Hörz, 1969), no

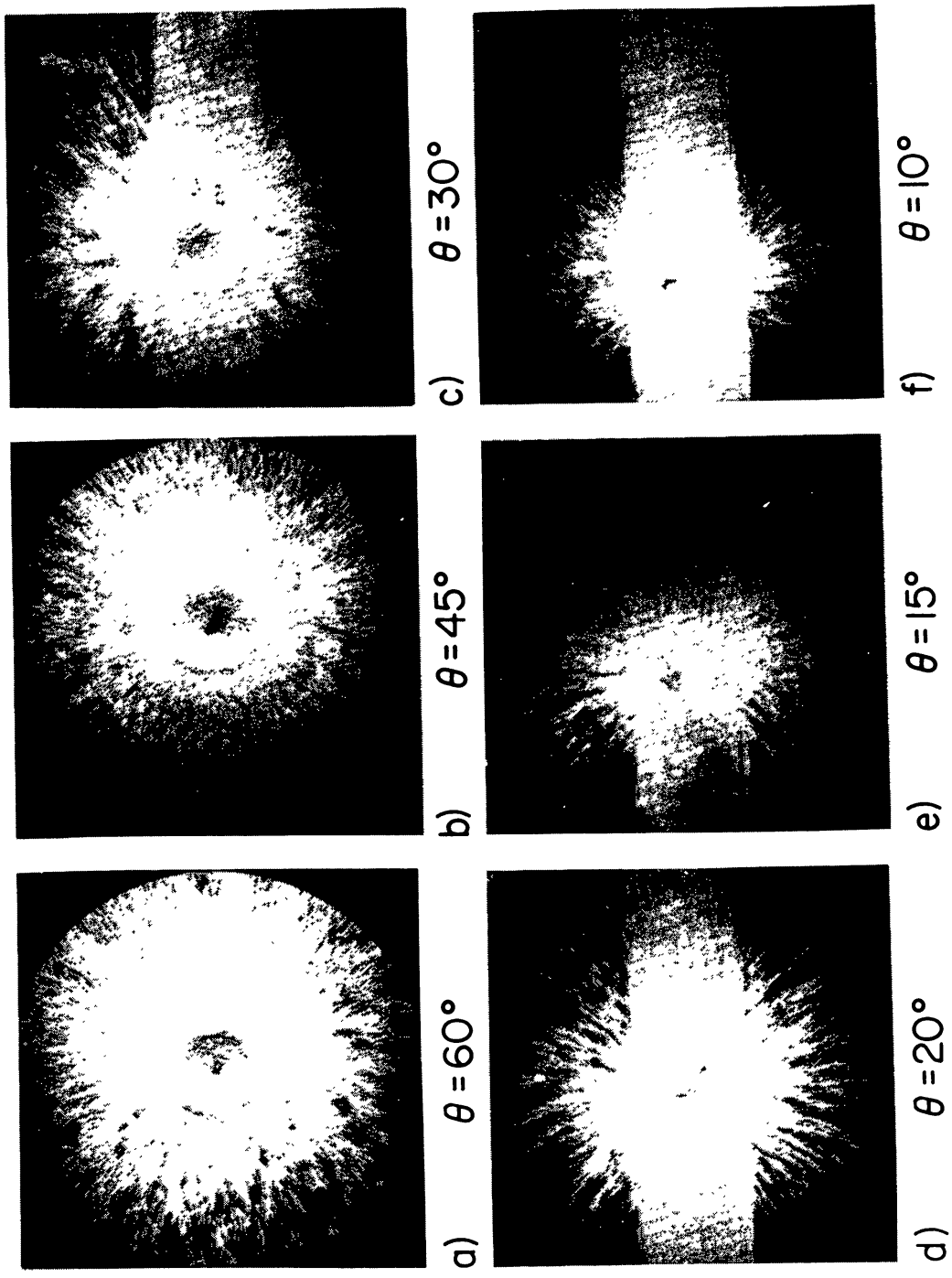

Fig. 10. Effects of oblique trajectory on distribution of ejecta around craters formed in pumice dust (<105 μm) by impacts of pyrex spheres at velocity approximately 6.4 km/sec. Trajectories from left to right.

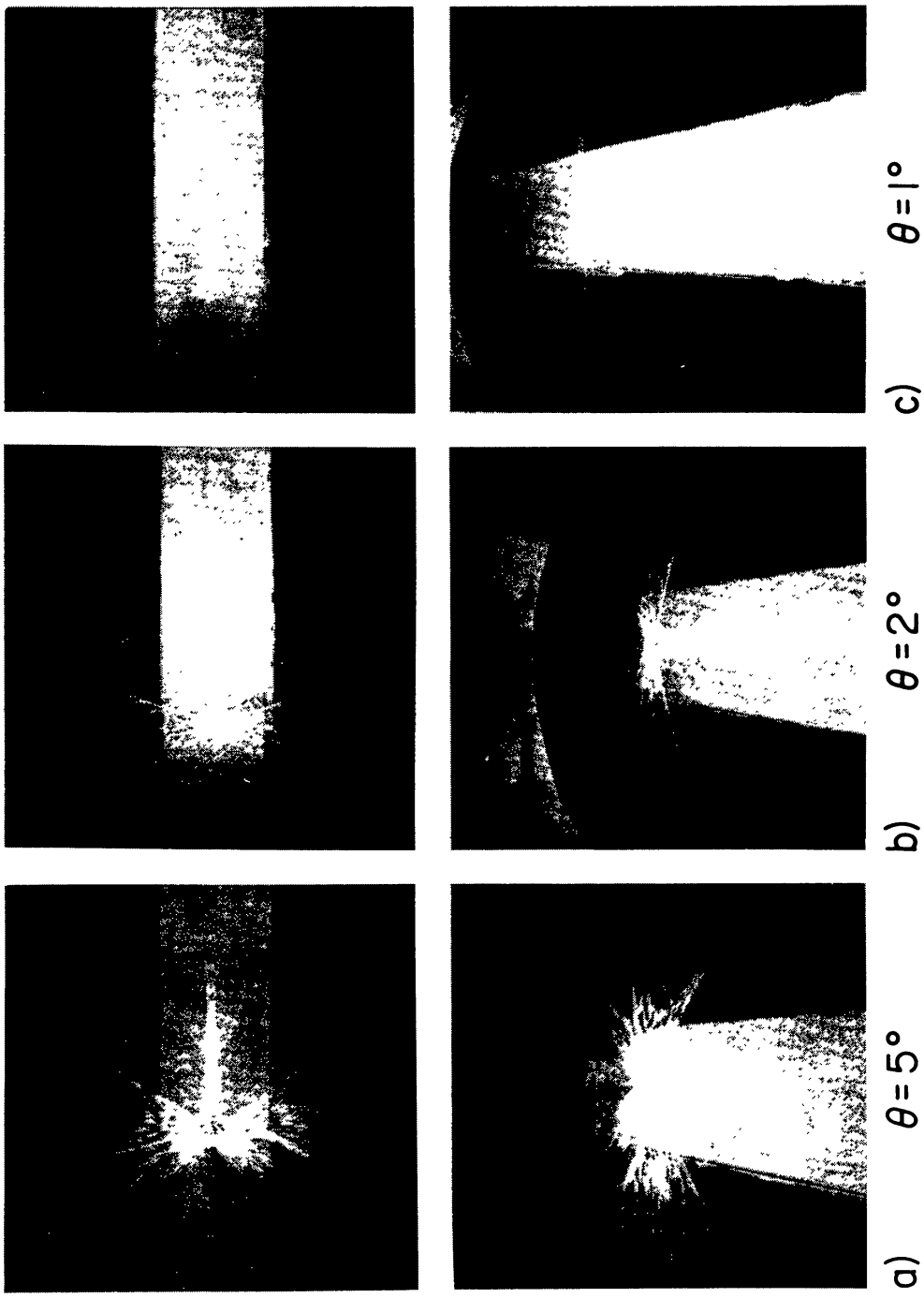

Fig. 11. Effects of oblique trajectory on distribution of ejecta around craters formed in pumice dust (<105 μm) by grazing impacts of pyrex spheres at velocity approximately 6.4 km/sec. Trajectories from left to right in top views and from top to bottom in bottom views.

meaningful details of final ejecta distribution are produced to model the terminal stages of ejection and deposition for large planetary cratering events. For craters formed in quartz sand and pumice, however, the terminal stages of ejection of the bulk of the displaced material, which forms the continuous deposits, maintains a slight downrange-tilt asymmetry of the ejecta plume. No major asymmetry has been observed in the final distributions of continuous ejecta deposits within the geometric limits of the experimental impact chamber (>3 crater diameters).

Decreasing θ to values less than 45° exagerates the preceeding effects and leads to highly asymmetric ejecta deposits displaying "forbidden" azimuthal zones. Figures 10 and 11 illustrate these effects of oblique trajectories for conditions of pyrex projectiles impacting pumice powder with velocities from 6.0 to 6.7 km/sec. With decreasing incidence below 45° a forbidden zone first appears uprange from the crater and then subsequently at shallower incidences a second zone appears downrange, both extending from the crater rims with bi-lateral symmetry about the path of the projectile trajectory. Similar ejecta patterns have been reported by Moore (1976) around craters formed by un-armed missile impacts ($\theta \approx 45°$) into soils at the White Sands Missile Range, New Mexico. For near grazing incidence the azimuthal extent of the forbidden zones expand to the degree that butterfly-wing-like deposition patterns are produced as a result of displaced material being ejected only at essentially right angles to the path of the projectile. In these extreme cases the projectile ricochets and may produce extensive downrange gouges (rays?).

Such bi-lateral symmetry around craters on planetary surfaces is a firm basis for recognizing structures formed from oblique trajectories and provides a basis for determining the direction of approach of the impacting object. In particular the similarity of the butterfly-wing patterns in Fig. 11 with those emanating from lunar crater Messier (Fig. 12) is striking and persuasive evidence for Messier's origin by a grazing impact event ($\theta < 5°$) of a body that approached from an easterly direction. Many additional examples of major oblique impacts on the moon are easily identified (e.g., Proclus, Tycho, Aristarchus, Kepler, etc.), but smaller events are also evident as shown in Figs. 13 and 14. Asymmetries are also observed around mercurian features, and recent Viking Orbiter photography has revealed some striking examples of oblique impacts on Mars (Figs. 15 and 16) for which the ejecta behaved in a fluidized manner (Carr *et al.*, 1976, 1977; see also Gault and Greeley, 1978).

MELT DISTRIBUTION

Target and projectile material that are melted as the result of impact shock heating respond and are ejected in a manner similar to the bulk of the displaced mass, although with some important differences. Downrange ejecta focusing of the melt products of the impacts is very well developed at $\theta = 45°$, although melt is ejected at other azimuths, including uprange, at greatly reduced amounts relative to the axial-symmetric conditions of vertical impact. Between $\theta = 45°$ and 90° focusing of melt downrange is greatest for the initial jetting mass (Gault *et al.*, 1963) and

Fig. 12. Lunar crater Messier (14 × 6 km) located in Mare Fecunditatis (48°E, 3°S) that displays the "butterfly wing" ejecta pattern deposits similar to those formed in the laboratory by impacts with trajectory angles $\theta<5°$. AS15-2403 photograph.

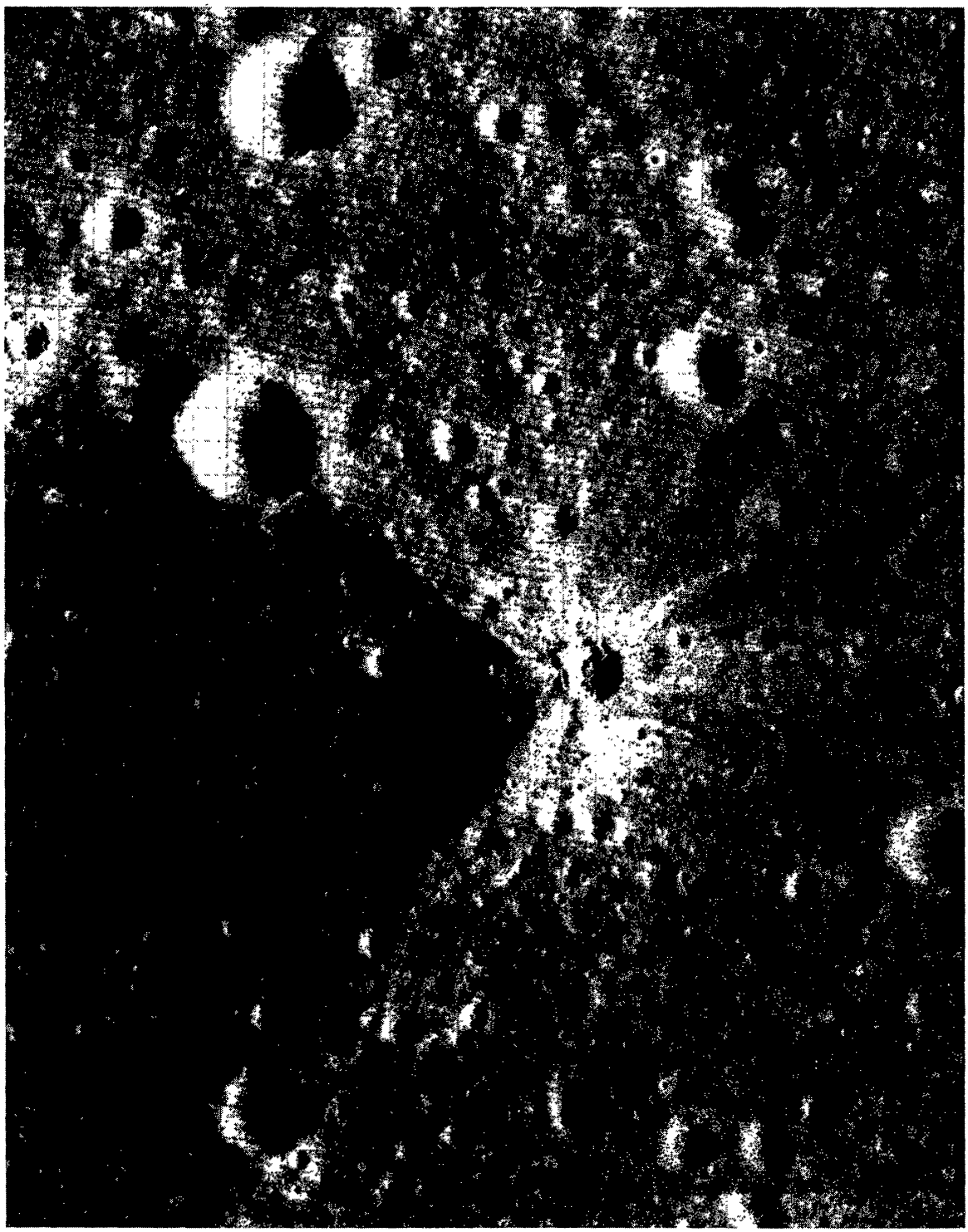

Fig. 13. Small (1 km) un-named lunar crater near 18°E, 25°N in Mare Serenitatis showing ejecta deposits with a "forbidden" zone similar to laboratory experiments for $\theta = 10° - 15°$. AS15-9337 photograph.

Fig. 14. Small, un-named, elongate (1 km) lunar crater that is a miniature version of Messier. Crater is west of Macrobius at 43°E, 20°N. AS15-9254 photograph.

Fig. 15. Viking Orbiter photograph of an un-named 10 km diameter martian crater at 259°W, 45°N on Utopia Planitia. Bilateral symmetry of ejecta deposits is similar to laboratory impacts with low incidence ($\theta<15°$?) for an object traveling from the southeast to northwest. Morphology of the deposits resembles martian ejecta deposits described by Carr *et al.* (1976, 1977) who suggest that the ejecta behaved as a fluidized mass due to entrained air and/or entrapped water or water vapor. Viking Orbiter frame 010B52.

subsequent highest-velocity components of ejecta. However, as the craters grow in size and the ejection velocities decay, melt is ejected throughout the 360° azimuthal range as it flows up from a "puddle" or reservoir of melt that lines the bottoms of craters at the steepest angles of incidence. The size or apparent volume of these reservoirs decreases rapidly with decreasing θ and the low-velocity ejec-

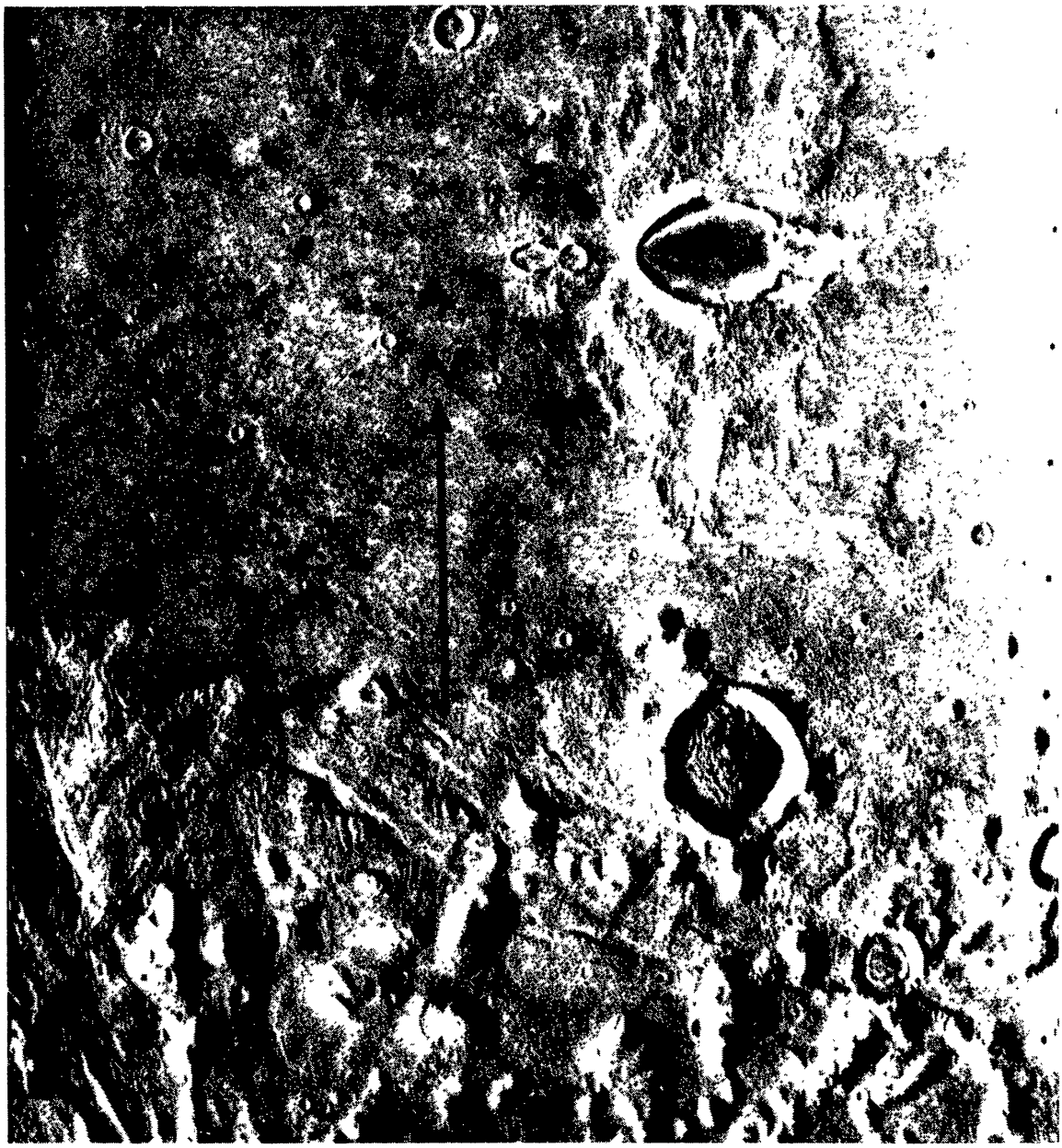

Fig. 16. Viking Orbiter photograph of a pair of un-named martian craters (12 × 8 km and 4 × 2 km) on the margin of Arcadia Planitia that are virtual twins to lunar crater Messier. Both craters, located at 138°W, 41°N, display "butterfly wing" ejecta patterns typically produced as the result of impacts from grazing trajectories ($\theta<5°$?). The trajectory alignment of the pair (West to East) suggests contemporary formation by two separate masses, possibly as the result of tidal disruption of a larger parent mass just prior to their impacts. Ejecta deposits evidence post-depositional flows as discussed by Carr *et al.* (1976, 1977). Viking Orbiter frame 039B13.

tion of melt in the uprange direction also decreases. For angles of θ less than 45° the downrange focusing of melt ejecta becomes very pronounced, even the lowest-velocity components, and at angles for incipient richochet and angles at grazing incidence the entire mass of melt produced by the impacts is ejected downrange

confined to a very narrow range of azimuthal angles.

This strong downrange focusing of melt ejecta is illustrated in Figs. 17 and 18, which present selected frames from movie records of the impacts of aluminum spheres into quartz sand at velocities from 6.0 to 6.3 km/sec. Unfortunately these black and white reproductions of the original records in color cannot show that most, if not all, of the early ejecta is incadescent and indicative of the liquidous state. Shown in Fig. 17 are the first or "impact" frames from the movie records. Direct temporal comparisons between individual frames is not possible because, for the framing rates of about 7000/sec, the actual times after impacts may vary as much as the inter-frame interval (140 μsec) between the different angles of obliquity. Moreover, it should be remembered that with an approximate shutter speed of 40 μsec, the high ejecta velocities cause extensive image smear and superposition so that the ejecta plume shapes have been "averaged" and appear fuzzy or nebulous. For example, although the ejecta velocities cannot be determined with any great precision, these and other similar records do serve to indicate the initial ejection velocities for all angles of θ are comparable to the impact velocity. Image motion registered on the "impact" frame of the movies, therefore, may be as great as 20–30 cm. The ejection velocities decay very rapidly, and Fig. 18 presents the corresponding second frames of the film records. Here image smear is, of course, still present, but greatly reduced and the "averaged" plume shapes are relatively undistorted from instantaneous, zero-smear shapes. The rapid change with θ from symmetric to downrange ejection of the melt is apparent. It is also to be noted that for all angles of obliquity the initial angles of ejection are less than those at later times. This generalization is best exemplified in Figs. 17 and 18 for $\theta = 90°$ to 45°; initial angles of ejection are less than 20° (Fig. 17) but they quickly steepen to 40°–50° (Fig. 18).

These observations of the behavior of melt within the craters and the mode of ejection are consistent with and support photogeologic interpretations of lavalike deposits around lunar craters. The lavalike materials appear to have been emplaced and flowed or ponded in a fluid state and occur around many, generally large, lunar craters. Although first interpreted to have a volcanic origin (e.g., Strom and Fielder, 1970) Shoemaker *et al.*, (1968) and Guest (1973) suggested that such materials around, respectively, Tycho and Aristarchus, are melt produced by shock-heating during the impact events that produced the craters. Moreover, Shoemaker *et al.* (1968) recognized the lavalike deposits were concentrated in the same direction as Tycho's prominent ray system, probably as the result of the oblique impact. Subsequently, Howard and Wilshire (1975) and most recently Hawke and Head (1977) have shown a strong correlation between locations of the melt concentrations and the azimuthal directions of the main crater ejecta deposits. Collectively, these photogeologic studies and the laboratory observations appear to be irrefutable evidence for an impact melt source for the lavalike materials. However, contrary to the model suggested by Hawke and Head (1977) for emplacement of large amounts of melt on crater rims, the laboratory results indicate such deposits can originate during oblique impact events as part of and accompanying the general sequence of ejection of the main mass from the crater of excava-

tion—and not at a later stage triggered by collapse of the rims of the transient crater of excavation.

RICOCHET

Richochet occurs for all low-angle impacts and includes, for present purposes, those conditions for which a significant fraction of the projectile rebounds from its initial point of contact against the target surface (i.e., the primary crater) and then continues in a ballistic or skipping trajectory along approximately the same azimuth(s) as the pre-impact trajectory. With this definition the richocheting projectile may have lost mass, fragmented, and the downrange trajectory (or trajectories) may or may not lead to additional cratering. These is no unique "critical" value of the trajectory angle for the onset of ricochet as θ is decreased. Except for special—generally low velocity—impacts, projectile material is always ejected (rebounds) during an impact event either as a solid, or in the liquidous or vaporous state at typical meteoritical velocities. As θ decreases the projectile material, in the same manner as the main mass of ejecta, tends preferentially toward downrange azimuths and eventually over an ill-defined but fairly narrow range of incidence ($\approx 15°$) assumes the concentrated downrange azimuthal trajectories of ricochet as defined. The onset of ricochet is, therefore, a transitional process and "critical angle" as used in the following is a subjective value. The subjectivity is complicated by the fact that in the transitional range for indentical given conditions the primary crater morphologies and downrange phenomena reproduce only in generalities.

The critical angle (range) of θ below which ricochet occurs depends on several variables including the impact velocity and the relative strengths and densities of the projectile and target materials. Although physical strength is probably of decreasing importance for typical lunar and planetary impact velocities when peak shock stresses are measured in megabar and tens of megabars, greater strength and/or density of the target (granite) relative to projectile (pyrex, plastics) serves to promote ricochet and lead to larger critical angles than when the projectile strength and/or density (all materials) are greater than the target (particulates). With rock targets in the laboratory, ricochet is imminent (Fe projectile) or commencing (pyrex, plastics) for $0 = 30°$ and is well developed at $\theta = 15°$ for all materials. The critical value of θ for ricochet from the particulates, however, is about 15° and full development occurs at angles less than 10°. Note in Fig. 4, moreover, that as the projectile density and/or strength is reduced from solid aluminum to hollow aluminum to pyrex, breakup and downrange "cratering" accompanying ricochet increases.

In order to examine the breakup, distribution, and trajectories of ricocheting projectile materials, a series of experiments were performed with aluminum "witness" plates positioned downrange of the primary craters. Figure 19 shows three such witness plates *in situ* after completion of the experiments and Figs. 20–24 show in detail selected plates for a range of incidences from 5° to 30° for aluminum

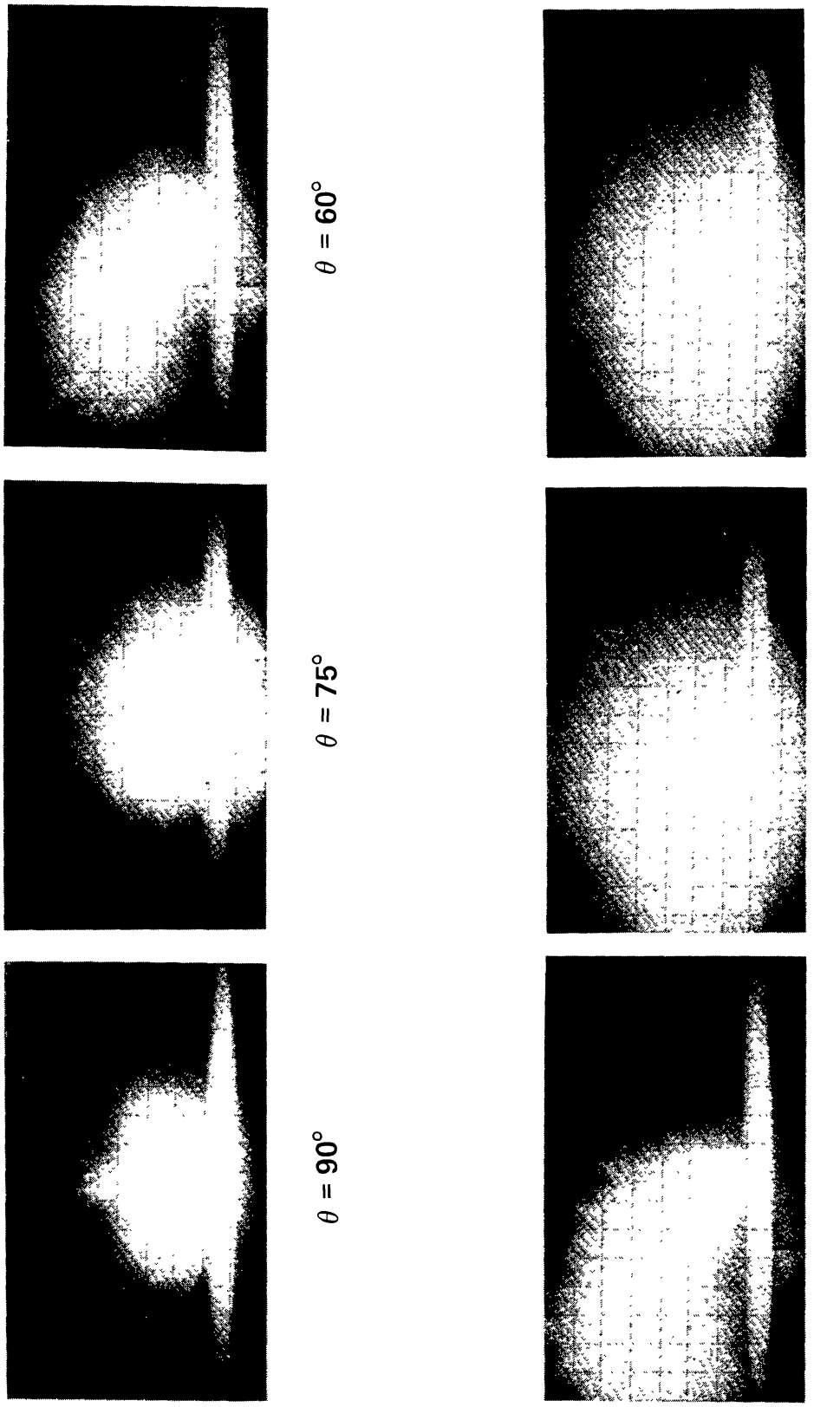

Fig. 17. First ("impact") frames of high-speed movie records (7000 frames/sec) of impacts of aluminum spheres into non-cohesive quartz sand with velocity 6.0 to 6.3 km/sec. Trajectories are from right to left; field of view is approximately 60 cm across at plane of the impacts.

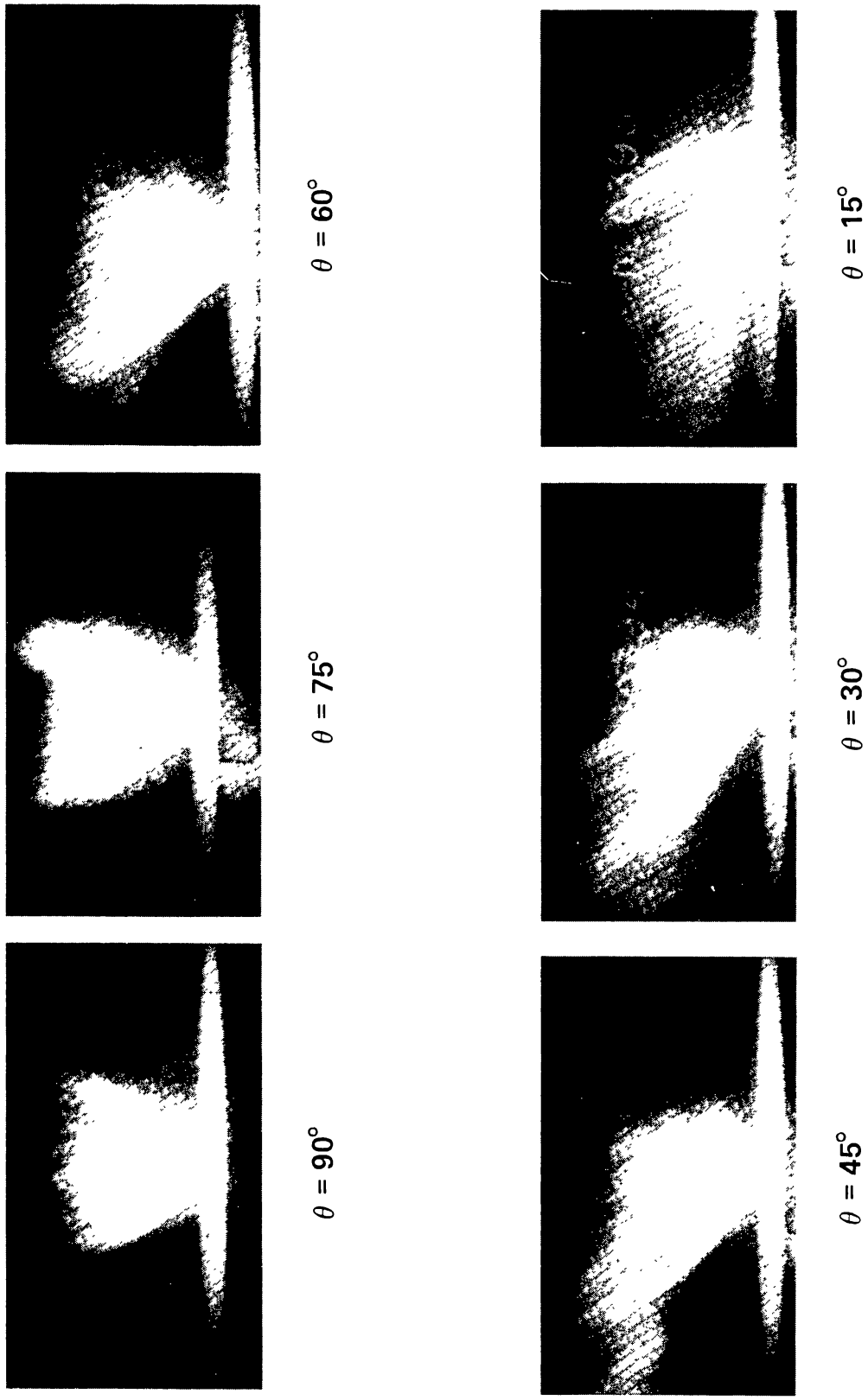

Fig. 18. Second frames after impacts (≈140 μsec) shown in Fig. 17.

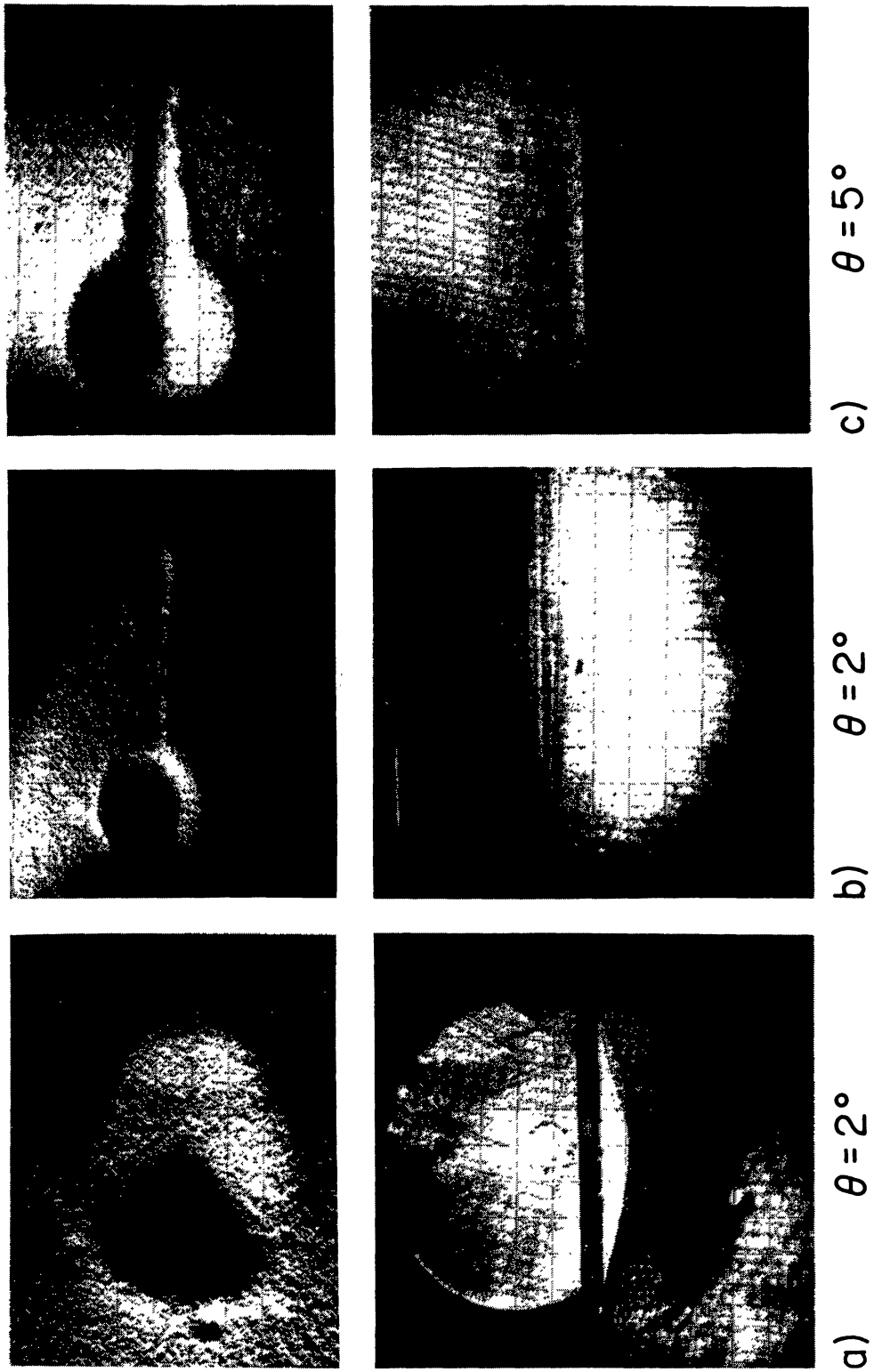

Fig. 19. Craters and downrange witness plates *in situ* after impacts into non-cohesive quartz sand. Disturbed region in sand below witness plates caused by ejecta from crater(s) formed in witness plates. a) aluminum sphere at 6.1 km/sec; b) pyrex sphere at 6.7 km/sec; c) pyrex sphere at 1.9 km/sec.

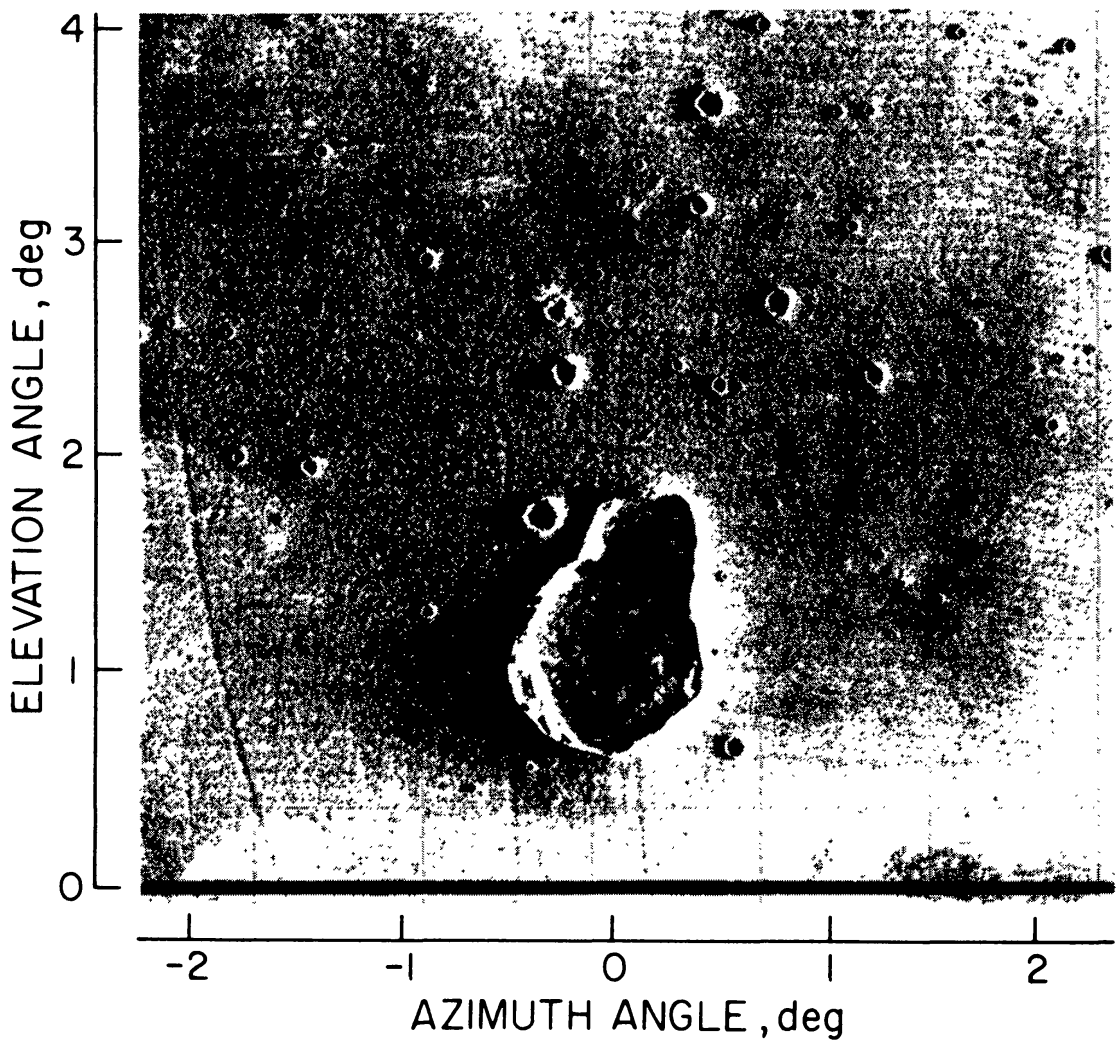

Fig. 20. Aluminum witness plate record for an aluminum sphere into non-cohesive quartz sand at 6.5 km/sec, $\theta = 4.75°$. Projectile fragmented into two main pieces and numerous fine particles. 1° in azimuth = 2.7 cm.

and pyrex projectiles. These records illustrate that dependent on the projectile material ricochet may occur either with the projectile remaining intact (Fig. 19a), rupture into several large fragments (Fig. 20), or shatter into a myriad small fragments (Figs. 19b, c and 21–24). The degree of breakup is greatest at the steepest (critical) angle for ricochet with fewer, larger fragments as incidence angle is decreased. The pyrex (brittle) projectiles shattered for all conditions of ricochet, but the aluminum (stronger, ductile) projectiles remained intact at grazing angles and experienced severe fragmentation only for steeper incidences. Fragmentation is, of course, promoted by increasing impact velocity. Aluminum projectiles survived essentially intact for an impact velocity of 1.8 km/sec at $\theta = 15°$ in contrast to the fragmented conditions shown in Fig. 21 for 6.3 km/sec; equivalent survival at the higher velocity occurred only for $\theta < 5°$. Increasing velocity also serves to decrease the ricochet angle-of-ejection from the primary crater, an effect which

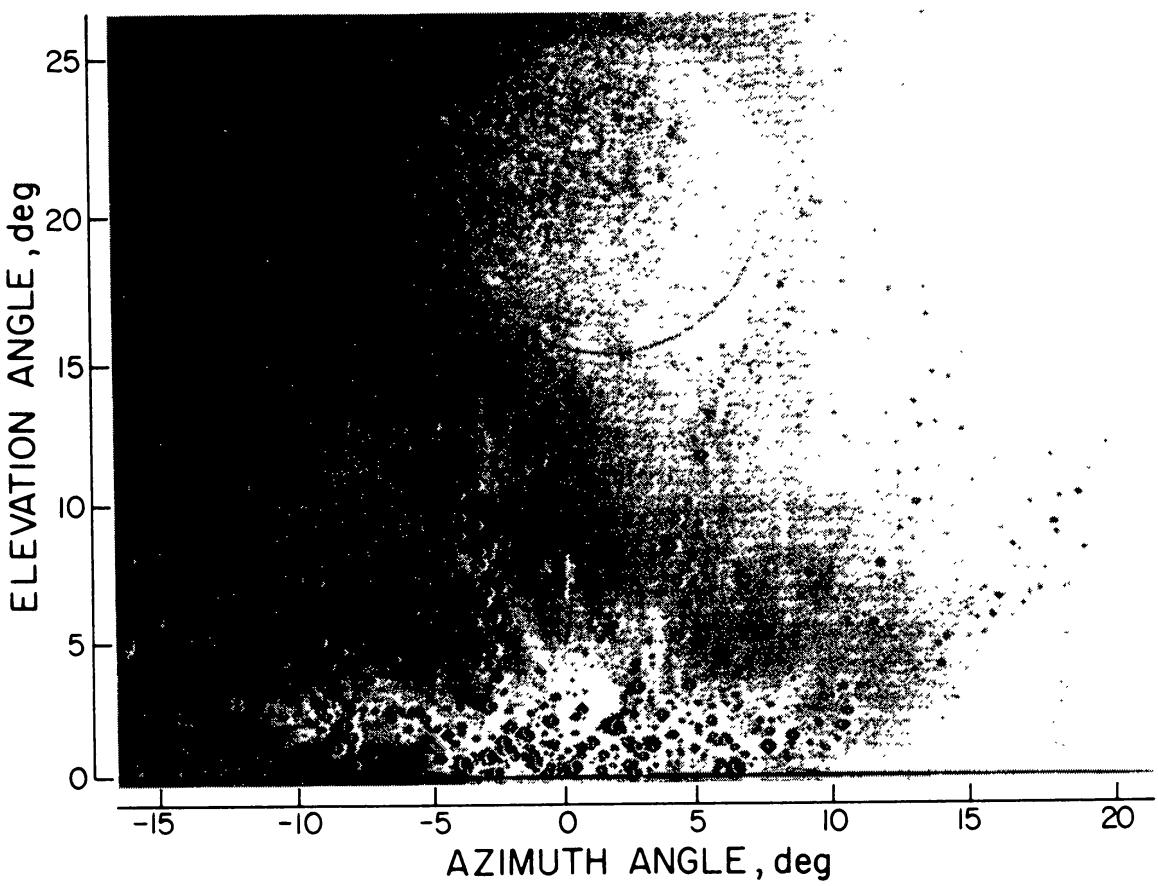

Fig. 21. Aluminum witness plate record for an aluminum sphere into non-cohesive quartz sand at 6.3 km/sec, $\theta = 15°$. Projectile fragmented into many small pieces concentrated into downrange trajectories with elevation angles less than about 2.5°. Note, however, the streaks of craters extending up to elevation angles from 15° to 20° (ray forming?). 1° in azimuth = 1.3 cm.

promotes cratering disturbances downrange from the primary. The ricochet ejection angle for the aluminum projectiles determined from witness plate records is presented as Fig. 25.

In addition to the major craters formed on the witness plates by projectile fragments, many fine, microscopic pits were produced and the entire surface of the plates lightly dusted with target materials, the latter clearly for impacts into quartz sand being some melt and primarily comminution products of the uprange impact. Because of the unavoidable superposed "contamination" by target material, it is not clear whether the pitting is caused by either fine projectile fragments or target particles accelerated during the primary impact (and downrange cratering) and entrained with the projectile fragments into downrange trajectories, or a mixture of both materials. The movie records clearly support high velocity downrange trajectories of target material, but quantitative measurements from the witness plates of the high-velocity mass are precluded by the trailing low-speed mass. Moreover, the source of any melt on the plates is uncertain, whether it is due to

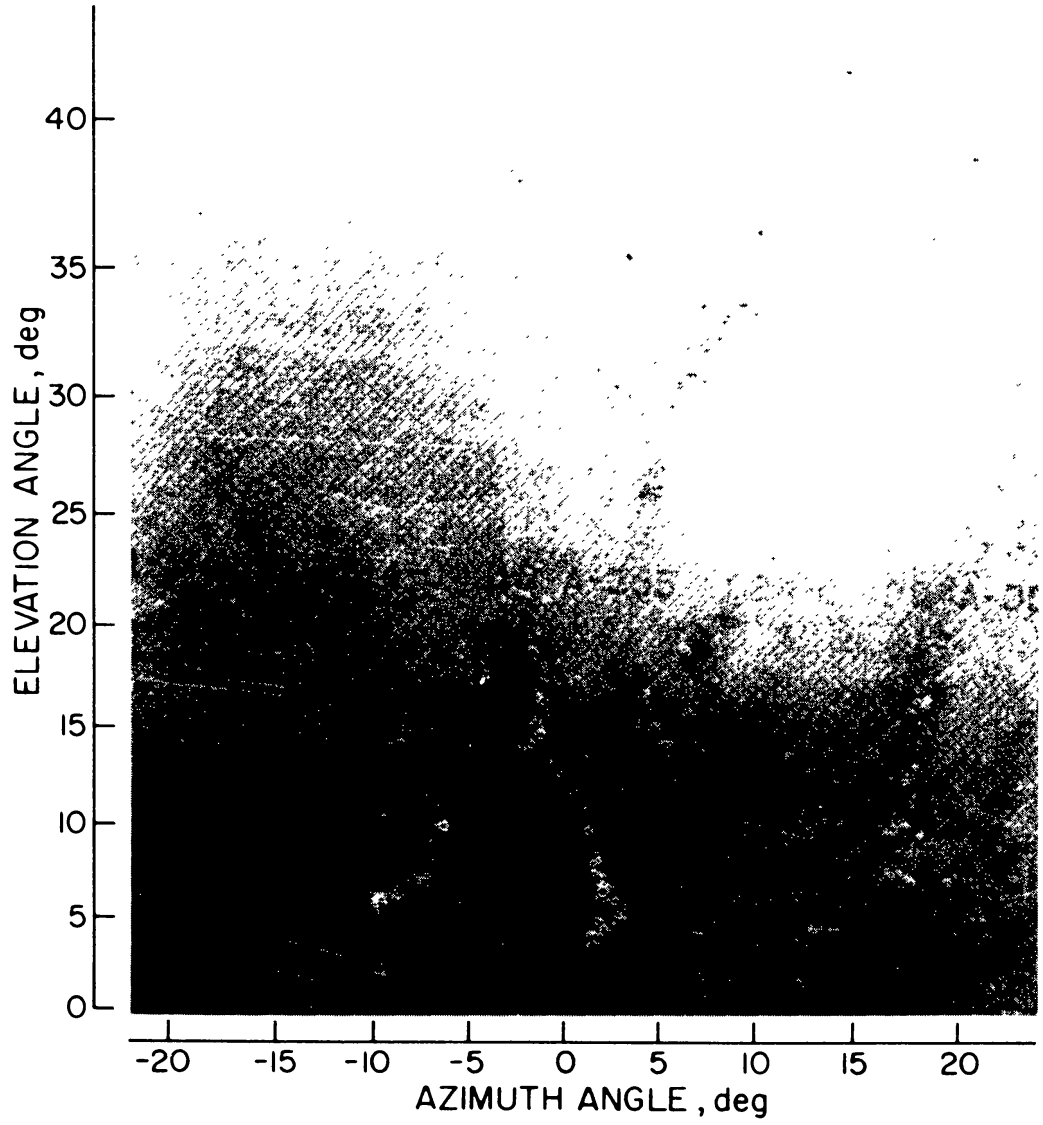

Fig. 22. Aluminum witness plate record for an aluminum sphere into non-cohesive quartz sand at 5.9 km/sec, $\theta = 30°$. Projectile shattered into innumerable fine fragments, all concentrated in primarily in three streaks having elevation angles greater than 5°. 1° in azimuth = 0.9 cm.

the primary impact, secondary impact on the witness plate, or possibly a combination of both impacts. The witness plate records, nevertheless, do provide a basis for estimating the velocity of the ricocheting projectile (fragments) and some limits on the velocity and mass of entrained target material carried downrange with the projectile.

To perform the witness plate analysis, starting from Eq. (4), write

$$\Delta m = m_{90°} - m_\theta = m_{90°}(1 - \sin^\delta \theta) \tag{9}$$

where Δm represents a mass of target material that was not displaced by an impact occuring in a trajectory with an angle θ relative to what could have been displaced

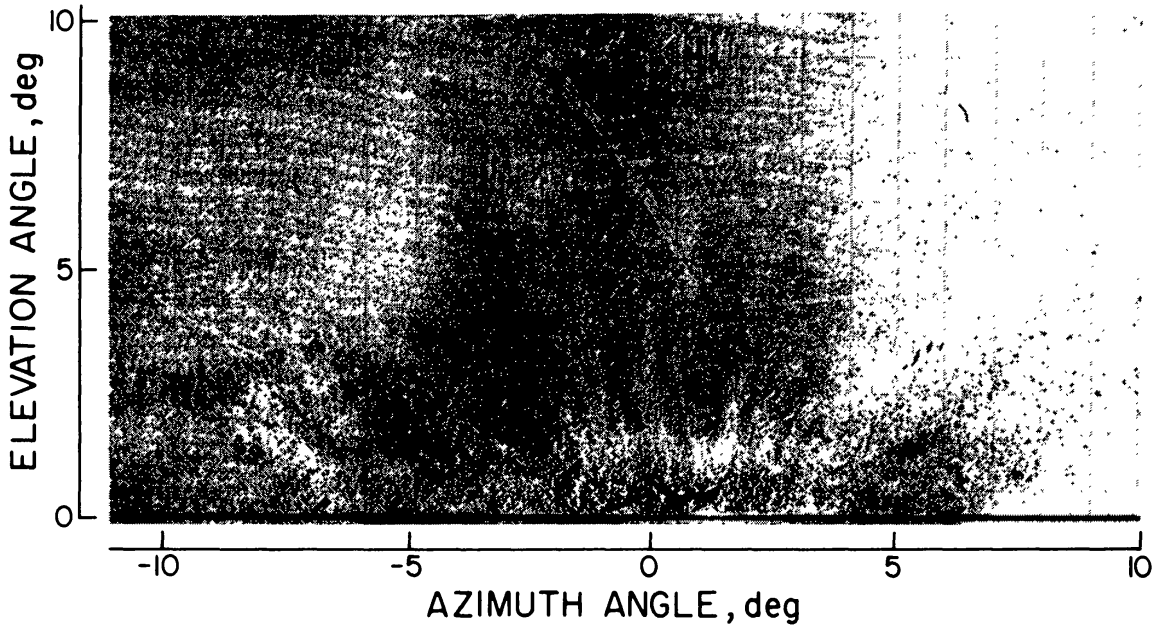

Fig. 23. Aluminum witness plate record for a pyrex sphere into non-cohesive quartz sand at 5.9 km/sec, $\theta = 7.3°$. Projectile shattered into a myriad of fine particles which, concentrated into a 3° × 1° downrange pattern of trajectories, produced overlapping craters and a jagged, irregular erosion hole. Compare with Figs. 19 and 20. 1° in azimuth = 1.3 cm.

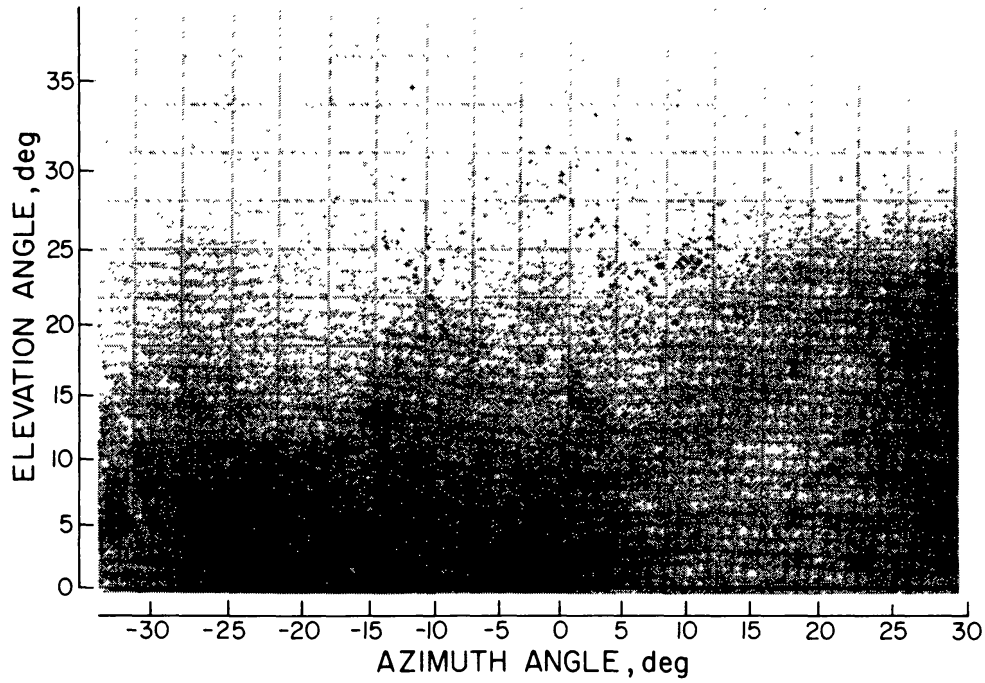

Fig. 24. Aluminum witness plate record for a pyrex sphere into non-cohesive quartz sand at 6.5 km/sec, $\theta = 30°$. Projectile disrupted into innumerable small particles that clustered into downrange trajectories above elevation angles of 10°. 1° in azimuth = 0.8 cm.

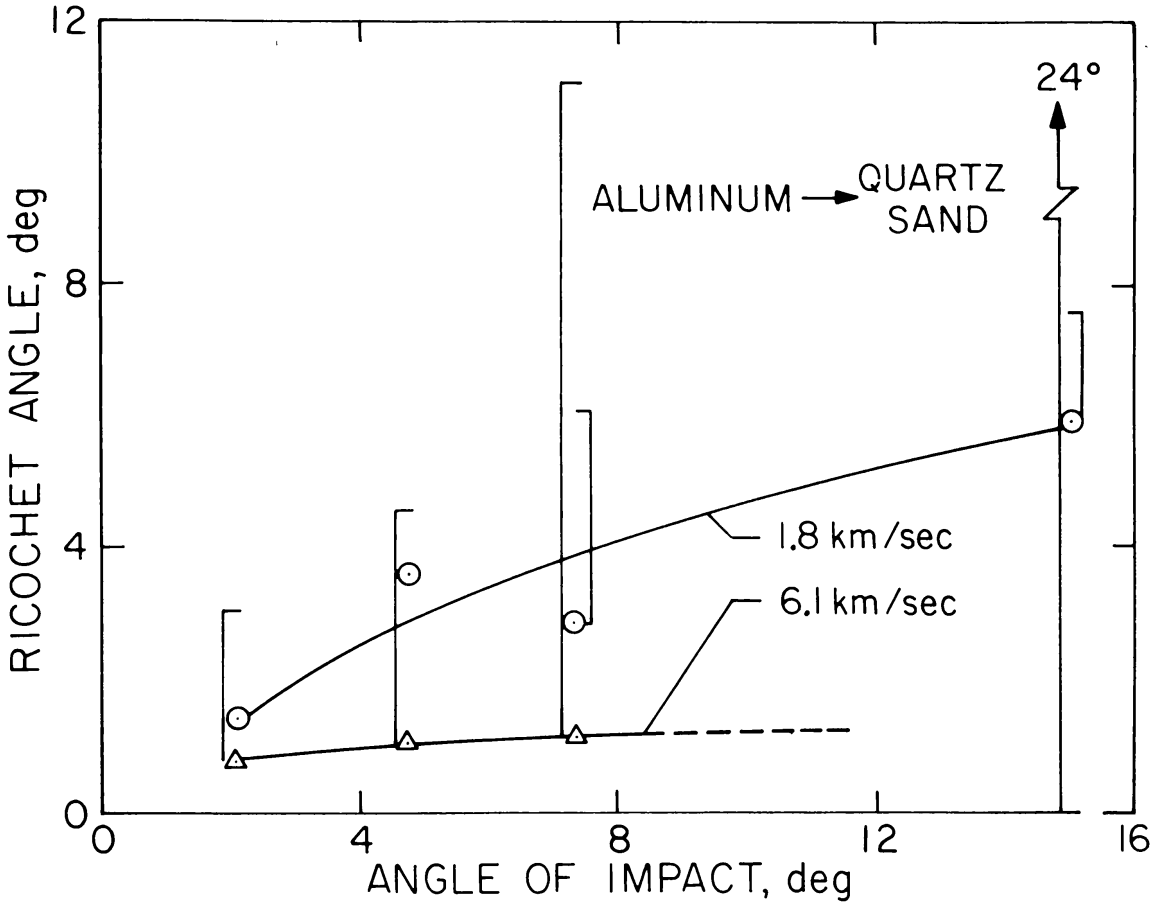

Fig. 25. Angle of ricochet from craters formed in non-cohesive quartz sand by aluminum spheres at velocities from 5.7 to 6.5 km/sec. Data points indicate main mass(es); barred lines indicate extent of scatter of the smaller fragments.

for $\theta = 90°$. In a similar manner one may write for the kinetic energy E

$$E_{90°} = E_\theta - E_r \tag{10}$$

That is, if the impact at angle θ has been produced, instead, by an event with $\theta = 90°$ the initial or total energy in the system could have been reduced by an amount equal to E_r. The energy E_r represents energy that was not expended for cratering and can be equated to the mass Δm that was not displaced. From (5)

$$m_{90°} \propto E_{90°}^{3\beta}$$

and

$$\Delta m \propto E_r^{3\beta}$$

so that Eq. (9) becomes

$$E_r = E_i(1 - \sin^\delta \theta)^{1/3\beta} \tag{11}$$

where the energy $E_{90°} = E_i$ is simply the kinetic energy $\frac{1}{2} m_p V_i^2$ of the impacting

projectile. Now the energy E_r is the sum of the kinetic energies of the ricocheting projectile E_{rp} and any entrained target material E_{rt} so that

$$E_r = E_{rp} + E_{rt} = \tfrac{1}{2}(m_p V_{rt}^2 + m_t V_{rt}^2)$$

and Eq. (11) may be recast into

$$(E_{rp} + E_{rt})/E_i = (1 - \sin^\delta \theta)^{1/3\beta} \tag{12}$$

and the equivalent expression for the velocity ratios is

$$(V_{rp}/V_i)^2 + (m_t/m_p)(V_{rt}/V_i)^2 = (1 - \sin^\delta \theta)^{1/3\beta} \tag{13}$$

More realistically, the ricochet energy E_r is the sum of many projectile fragments and target particles, each having different velocities, so that the parameters in Eqs. (12) and (13) should be interpreted to be mean or integrated averages.

Denardo *et al.* (1967) present results from an extensive series of experiments for 1.6 to 12.7 mm diameter aluminum spheres impacting with velocities up to 8.6 km/sec into aluminum targets of the same type employed in these witness plate experiments. The results from the studies of Denardo *et al.* (1967) permit conversion of the witness plate cratering records to the kinetic energy retained by the ricocheting projectile fragments. Results derived from the witness plate craters in this manner are presented in the accompanying table together with comparisons with values obtained from Eqs. (11), (12) and (13).

The experimental values of the projectile ricochet energy ratio E_{rp}/E_i are all smaller than the values for the available amounts E_r/E_i calculated from Eq. (11). The smaller experimental values and their trend to proportionately greater differences from the calculated values as θ increases are consistent with the acceleration and entrainment ejection of increasing masses of target material along with the ricocheting projectile. An expression for the entrained mass m_t can be obtained by rearranging Eq. (13)

$$m_t/m_p = (V_{rp}/V_{rt})^2[1 - (E_i/E_{rp})(1 - \sin^\delta \theta)^{1/3\beta}] \tag{14}$$

but without some knowldege of the velocity ratio V_{rp}/V_{rt} no estimate is possible. If one assumes for simplicity that projectile and target material have equal velocities $V_{rp} = V_{rt}$, the values listed in the table result from Eq. (14). These values, however, are believed to be extremely conservative. Although some target material attains very high velocities, as indicated by the high speed framing camera records, a lower velocity component trails behind. Because the mass m_t varies inversely with the square of its (mean) velocity, the entrained mass can be considerably greater than the tabulated values. Unfortunately, the present results are inadequate to clarify this point, and better definition of the ejected (entrained) masses depends on more detailed and refined experiments.

These witness plate results point to some interesting (and speculative) possibilities of planetary cratering events which must have occurred throughout solar system history—that is, meteoritic objects have cratered the surfaces of even the largest atmosphere-free bodies and then accompanied with some entrained materials from the bodies ricocheted back into heliocentric space. For example, the

Table I. Witness Plate Results

θ	V_i (km/sec)	N*	E_{rp}/E_i (Exp.)	E_r/E_i (Eq. 11)	E_{rp}/E_r	m_t/m_p (Eq. 14)	V_{rp}/V_i (Eq. 13)
2.12	6.13	1 + 0	0.81	0.93	0.87	0.15	0.91
4.75	6.52	2 + 0	.77	.84	.92	.09	.88
7.33	5.71	1 + 7	.67	.76	.88	.13	.82
15.0	6.28	0 + 29	.15	.55	.27	3.7	.39
30.0	5.95	0 + 62	.04	.25	.16	6.3	.20

*N denotes number of craters used to determine values of E_{rp}/E_i; first digit indicates largest craters responsible for major contribution to E_{rp} and second value designates number of smaller craters included, none of which made a major individual contribution but collectively contributed to the final amounts indicated.

values of V_{rp}/V_i listed in the table for angles of incidence $\theta < 10°$ allow ricochet for impact velocities as small as approximately 3 and 7 km/sec for, respectively, the moon and Mercury with subsequent escape from their gravitational fields. Satellites in decaying orbits around their parent body also would provide a source of ricocheting objects although not into heliocentric space after impact.

Results with pyrex projectiles clearly suggests that stoney or cometary objects could not survive any grazing impacts without total fragmentation even for such modest velocities that are much less than "typical" for the moon and Mercury from heliocentric space. The results with aluminum projectiles in the laboratory, however, does suggest that nickle-iron objects could survive a glancing event. The greater strength of nickle-iron will, in itself, greatly enhance the possibility of survival. Additionally, scaling up from the laboratory to larger, major-crater forming objects should be favorable for survival because body forces arising from deceleration during impact vary inversely with scale (size) while the peak shock (i.e., deformation) stresses are, to first order independent of scale. As a result, larger projectiles behave as though they are stronger than small ones—a result observed in the laboratory experiments with aluminum projectiles; 12.7 mm diameter spheres experience the same degree of deformation as 1.6 mm spheres only when their impact velocities are 50-percent greater.

Lunar crater Messier is, of course, the prime type-example of an oblique impact along a grazing trajectory for which projectile and accompanying lunar material must be expected to have ricocheted free of the moon's gravitational environment. If the impacting object had struck near the vertical, Messier today would be instead a circular structure enlarged from its original 30–40 km diameter crater of excavation to perhaps 40–50 km after collapse of the rim to form the interior terracing characteristic of large craters. Proclus and Tycho are also examples of potentially ricocheting lunar impacts, but as illustrated by Fig. 14, such events also occurred for smaller objects which are more frequent but because of the smaller size more easily eroded and lose their identity. Moreover, ricocheting impacts on Mars (Figs. 15 and 16) suggest similar possibilities and behavior if the objects are

sufficiently massive to preclude appreciable aerodynamic braking. For ricocheting hits on Mars and Mercury the escaping masses eventually have probably been swept up by the planets, but for lunar impacts there is the tantalizing possibility that earth has acquired significant amounts of lunar material in the past well before the Apollo missions.

Acknowledgments—We thank M. H. Carr and R. Greeley for bringing to our attention the evidence of grazing impacts captured by the Viking Orbiter imagery. One of us (DEG) wishes particularly to express his appreciation to the Sherman Fairchild Foundation for support while he was at the California Institute of Technology. We also thank F. M. Sauer and D. A. Morrison for their helpful reviews and comments.

REFERENCES

Baldwin R. B. (1963) *The Measure of the Moon*. Univ. Chicago Press, Chicago. 488 pp.

Barringer D. M. Jr. (1927) The meteor crater of Arizona: II The most fascinating spot on earth. *Sci. Amer.*, **137,** 144–146.

Bryan G. M. and Pugh E. M. (1962) Cratering of lead by oblique impacts of hypervelocity steel pellets. *J. Appl. Phys.* **33,** 374–378.

Carr M. H., Crumpler L. A., Cutts J. A., Greeley R., Guest J. E. and Masursky H. (1977) Martian craters and emplacement of ejecta by surface flows. *J. Geophys. Res.* **82,** 4055–4065.

Carr M. H., Masursky H., Baum W. A., Blasius K. R., Briggs G. A., Cutts J. A., Duxbury T., Greeley R., Guest J. E., Smith B. A., Soderblom L. A., Ververka J. and Wellman J. B. (1976) Preliminary results from the Viking Orbiter imaging experiments. *Science* **193,** 766–776.

Charters A. C. and Curtis J. S. (1962) High velocity guns for free flight ranges. TM 62-207, General Motors Corp. Defense Res. Lab., Santa Barbara, California, 73 pp.

Curtis J. S. (1964) An analysis of the interior ballistics of the constant base pressure gun. TM 64-27, General Motors Corp. Defense Res. Lab., Santa Barbara, California, 52 pp.

Denardo B. P., Summers J. L. and Nysmith C. R. (1967) Projectile size effects on hypervelocity impact craters in aluminum. NASA TN D-4067.

Fechtig H., Gault D. E., Neukum G. and Schneider, E. (1972) Laboratory simulation of lunar craters. *Naturwissenschaften* **59,** 151–157.

Fudali R. F. and Chapman D. R. (1975) Impact survival conditions for very large meteorites, with special reference to the legendary chinguetti meteorite. In *Smithsonian Contrib. Earth Sci. No 14*, (G. S. Switzer ed.), p. 55–62. Smithsonian Press, Washington, D.C.

Gault D. E. (1973) Displaced mass, depth, diameter, and effects of oblique trajectories for impact craters formed in dense crystalline rocks. *The Moon* **6,** 32–44.

Gault D. E. (1974) Impact craters. In *A Primer in Lunar Geology* (R. Greeley and P. Schultz eds.), p. 137–175. NASA TMX 62359.

Gault D. E. and Greeley R. (1978) Exploratory experiments of impact craters formed in viscous-liquid targets: Analogs for martian rampart craters? *Icarus*. **34,** p. 486–495.

Gault D. E., Hörz F., Brownlee D. E. and Hartung J. B. (1974) Mixing of the lunar regolith. *Proc. Lunar Sci. Conf. 5th,* p. 2365–2386.

Gault D. E., Hörz F. and Hartung J. B. (1972) Effects of microcratering on the lunar surface. *Proc. Lunar Sci. Conf. 3rd,* p. 2713–2734.

Gault D. E., Quaide W. L. and Oberbeck V. R. (1965) Interpreting ranger photographs from impact cratering studies. In *The Nature of the Lunar Surface* (W. N. Hess, D. H. Menzel, and J. A. O'Keefe eds.), p. 125–140. The Johns Hopkins Press, Baltimore.

Gault D. E., Shoemaker E. M. and Moore H. J. (1963) Spray ejected from the lunar surface by meteoroid impact. NASA TN D-1767

Gilbert G. K. (1893) The moon's face, a study of the origin of its features. *Bull. Philos. Soc. Wash.* (D.C.) **12,** 241–292.

Guest J. E. (1973) Stratigraphy of ejecta from the lunar crater Aristarchus. *Bull. Geol. Soc. Amer.* **84,** 2873–2894.

Hawke B. R. and Head L. W. (1977) Impact melt on lunar crater rims. In *Impact and Explosion Cratering* (D. J. Roddy, R. O. Pepin, and R. B. Merrill eds.), p. 815–841. Pergamon, N.Y.

Howard K. A. and Wilshire H. G. (1975) Flows of impact melt at luanr craters. *J. Res. U.S. Geol. Survey* **3,** 237–251.

Hörz F. (1969) Structural and mineralogical evaluation of an experimentally produced impact crater in granite. *Contrib. Mineral. Petrol.* **21,** 365–377.

Moore H. J. (1968) Ranger VIII and gravity scaling of lunar craters. *Science* **159,** 333–334.

Moore H. J. (1976) Missile impact craters (White Sands Missile Range, New Mexico) and applications to lunar research. *U.S. Geol. Survey Prof. Paper 812-B.* 47 pp.

Oberbeck V. R. (1971) Laboratory simulation of impact cratering with high explosives. *J. Geophys. Res.* **76,** 5732–5749.

Partridge W. S. and Van Vleet H. B. (1958) Similarities between lunar and high velocity impact craters. *Astrophys, J.* **128,** 416–419.

Rinehart J. S. and White W. C. (1951) Shapes of craters formed in plaster of paris by ultra-speed pellets. *J. Appl. Phys.* **22,** 14–18.

Roddy D. J. (1977) Large-scale impact and explosion craters: comparisons of morphological and structural analogs. In *Impact and Explosion Cratering* (D. J. Roddy, R. O. Pepin, and R. B. Merrill eds.), p. 185–246. Pergamon, N.Y.

Sabaneyev P. F. (1953) On the origin of lunar craters. *Vsesoyuzhoye Astonomo-Geodicheskoye Obshehestvo,* **13,** 20, 7–20 (Translated from the original Russian by Leo Kanner Associates, P. O. Box 5187, Redwood City, CA 94063).

Shoemaker E. M. (1962) Interpretation of lunar craters. In *Phys. and Astron. of the Moon* (Z. Kopal ed.), p. 283–359. Academic Press, N.Y.

Shoemaker E. M., Batson R. M., Holt H. E., Morris E. C., Rennilson J. J. and Whitaker E. A. (1968) Television observations from Surveryor VII. In *Surveyor VII Mission report, Part II, Science results*, p. 9–76. NASA TR 32-126.

Stöffler D., Gault D. E., Wedekind J. and Polkowski G. (1975) Experimental hypervelocity impact into quartz sand: Distribution and shock metamorphism of ejecta. *J. Geophys. Res.* **80,** 4062–4077.

Strom R. G. and Fielder G. (1970) Multiphase eruptions associated with Tycho and Aristarchus. *Commun. Lunar and Planetary Lab.*, Univ. Arizona **8,** 235–288.

Summers J. L. (1959) Investigation of high-speed impact: Regions of impact and impact at oblique angles. NASA TN D-94.